2015

Study of electronic characteristics of heterojunction with intrinsic thin-layer devices and defect density profile of nanocrystalline silicon germanium devices

Watson Paul Mulder
Iowa State University

Study of electronic characteristics of heterojunction with intrinsic thin-layer devices and defect density profile of nanocrystalline silicon germanium devices

by

Watson Mulder

A thesis submitted to the graduate faculty

in partial fulfillment of the requirements for the degree of

MASTER OF SCIENCE

Major: Electrical Engineering

Program of Study Committee:
Vikram Dalal, Major Professor
Rana Biswas
Mani Mina

Iowa State University

Ames, Iowa

2015

TABLE OF CONTENTS

LIST OF FIGURES

Page

LIST OF TABLES

ACKNOWLEDGMENTS

I would like to thank my major professor, Dr. Vikram Dalal, for his guidance and support for the last several years. His encouragement and faith in me were the primary inspiration for me to attend graduate school. This thesis would not have been possible without his support and direction, and it was an honor to work in his research group. I would also like to extend my thanks to my committee members, Dr. Rana Biswas and Dr. Mani Mina, for their efforts and contributions. I would like to acknowledge the support of NSF and the DOE Sunshot Initiative.

I would like to extend deepest thanks to Max Noack for his insightful discussions and help with experimental measurements and equipment, on numerous occasions. I would also like to thank Wai Leung for his help in the lab. I would like to thank Dr. Gary Tuttle for his perspicacious discussions and his inspiration to work in the field of semiconductor fabrication. I would like to thank Dr. Siva Konduri for training me on the reactors and teaching me various measurement techniques. I would like to extend thanks to Mehran Samiee for his helpful discussions and aid with various experiments. I would also like to acknowledge the help and insight of Dr. Dipak Paramanik in fabrication of devices. I would like to thank Hisham Abbas for his assistance and thought-provoking discussion.

I would like to thank Pranav, Ranjith, Balaji, Liang, Istiaque, Satvik, Andrew, and other former and current MRC graduate and undergraduate students who have always been helpful. In addition, I would like to thank my parents and the rest of my family for their moral support, motivation, and encouragement that made it possible for me to complete my graduate degree.

ABSTRACT

Heterojunction with Intrinsic Thin-layer (HIT) solar cells are an important photovoltaic technology, recently reaching record power conversion efficiencies. HIT cells hold advantages over the conventional crystalline Si solar cells, such as their fabrication at lower temperatures and their shorter fabrication time. It is important to understand the electronic characteristics and transport properties of HIT cells to continue to improve their efficiencies. The fundamental measurements of a HIT solar cell with an innovative n+/p/p+ structure are presented. We also report on a series of these HIT cells fabricated on wafers with different doping concentrations, observing the relationship between doping concentration and characteristics such as open-circuit voltage and diffusion length.

Nanocrystalline Silicon-Germanium (nc-SiGe) is a useful material for photovoltaic devices and photodetectors. The material features good absorption extending to the infrared region even in thin layers. Its bandgap can be adjusted between that of Si (~1.1 eV) and Ge (~0.7 eV) by varying the alloy composition ratio during deposition. However, there has been very little previous work to measure and understand the defect density spectrum of nc-SiGe. Defects are responsible for controlling the recombination and thus the performance of solar cell devices. Capacitance-Frequency measurements at various temperatures are used in order to estimate the trap density profile within the bandgap of nc-SiGe.

CHAPTER 1: INTRODUCTION

1.1 Solar Energy

Solar energy continues to become more important in our world as a vital renewable energy source. As the world reduces its reliance on fossil fuels and relies more on renewable energy, the use of solar energy is ever becoming more widespread and popular. It is not highly dependent upon location as are other renewable energy sources like wind and hydroelectric. On the contrary, solar energy is widely accessible around the globe, and many technologies are available to harvest this energy. Of particular interest is photovoltaic (PV) energy conversion, which is a means of converting solar energy into electricity. In PV conversion, a semiconductor material absorbs the incoming photons and converts the energy into electrons and holes. The charge carriers are separated by a p-n junction, creating a voltage and a current, which can be used to power a load. The primary challenge in photovoltaics is being able to obtain efficient energy conversion at an adequately low cost.

The costs of photovoltaic devices have been lowered somewhat due to developments in technology and production; however, there is still work to be done to further reduce costs to where photovoltaics are feasible as an alternative to fossil fuels. Solar energy certainly has the capacity to fulfill mankind's energy needs: nearly 70,000 Terawatts of solar energy reaches the earth each year. The world's annual energy consumption is a comparatively miniscule 20 Terawatts. Clearly, solar energy possesses outstanding potential to provide the entire earth with a clean, easily accessible renewable energy source. Moreover, photovoltaics is drawing great interest from researchers worldwide as a rapidly growing global industry. Photovoltaic global

capacity has ascended on an exponential growth curve over the past decade, achieving a total of 177 Gigawatts in 2014 as shown in Figure 1.1.

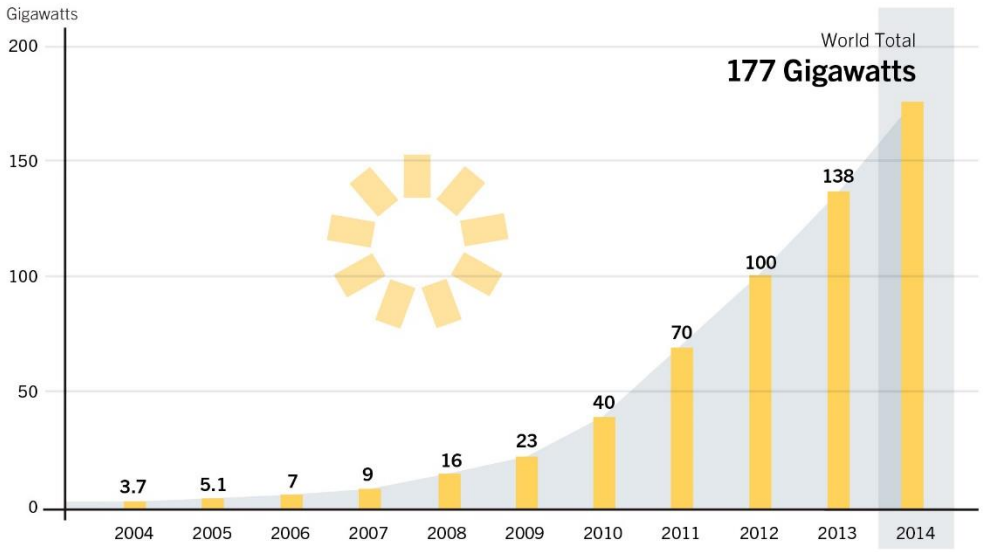

Figure 1.1 Photovoltaic global capacity over the last decade [1]

1.2 Forms of Silicon Used in Solar Cells

Silicon is the most widely used material to make solar cells and it takes several different forms. Figure 1.2 shows a visualization of the atomic structure of the forms of silicon. Crystalline silicon (c-Si) is the most common technology for use in silicon solar cells. Crystalline silicon enjoys widespread applications due to its relatively high efficiency and the predominance of the silicon industry.

Another widely used material is amorphous silicon (a-Si), which features an easy roll-to-roll production process and ease of deposition. Amorphous silicon has a highly disordered structure, and thus suffers from defects within the bandgap due to broken Si-Si bonds. However, a-Si can be passivated with hydrogen, causing many of the broken bonds to make a covalent bond with H and reducing the defect density very substantially [2]. This is why a-Si is often referred to as “a-Si:H”; the H indicates hydrogenation. Amorphous silicon does offer

advantages, such as a favorable bandgap energy (near the ideal bandgap for maximum solar energy efficiency) and high absorption coefficient [3]. A major disadvantage is the high defect density and low carrier lifetime, leading to a limited power conversion efficiency on the order of ~10%. These and other issues have prevented the widespread use of a-Si. The technology is now primarily targeted for use in tandem cells [4]. Heterojunction with intrinsic thin-layer (HIT) solar cells are an important technology in which thin layers of a-Si are deposited on a c-Si wafer. This is discussed in more detail in Chapter 2.

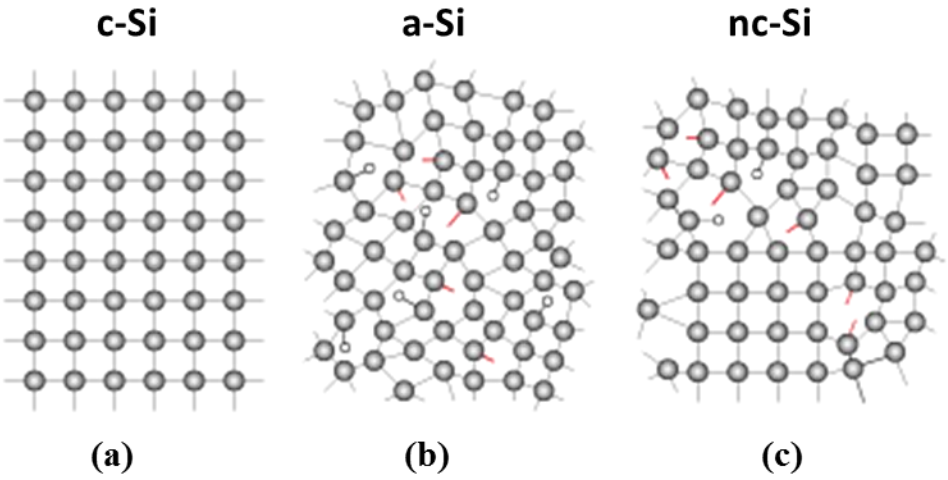

Figure 1.2 The different forms of silicon [5]

Nanocrystalline silicon (nc-Si) is a form of polycrystalline silicon that has fewer defects than a-Si [6]. It is so named due to the nanoscale grain sizes, although it is sometimes referred to as microcrystalline silicon; microcrystalline silicon more accurately refers to silicon with grains in the micrometer range. The structure of nc-Si is composed of tiny crystalline grains (approx. 10-20 nm) which are surrounded by amorphous tissue. As with a-Si:H, hydrogen is important for passivating the dangling bonds to reduce the defects, and the hydrogenated material is known as nc-Si:H. This helps to ensure that carriers can pass from one grain to the next without recombination occurring. This is necessary to achieve high efficiencies [7].

Nanocrystalline silicon growth hinges on an incubation layer and nucleation sites. The incubation layer is an amorphous layer with crystallites growing in conical shapes from the nucleation sites. The initial nucleation is dependent on the hydrogen dilution, which is the ratio of the hydrogen gas flow to the silane gas flow. Nanocrystalline silicon can be alloyed with germanium (nc-SiGe), which can be useful for bandgap flexibility and improved absorption. This is discussed in more detail in Chapter 3.

1.3 Structure of the Thesis

The objective of this work is to understand the fundamental properties of n+/p/p+ HIT solar cells and to investigate the defect density profiles of nc-SiGe solar cells. Chapter 1 contains an introduction to solar energy and a brief discussion about silicon solar cell technologies. Chapter 2 discusses HIT solar cells. Section 2.1 gives an introduction to HIT cells, and previous work on HIT is discussed in Section 2.2. Sections 2.3 and 2.4 detail the fabrication and measurement techniques, respectively, for HIT devices. Section 2.5 discusses results from the fabricated n+/p/p+ HIT cells, comparing results from devices with different base doping concentrations. Chapter 3 focuses on nc-SiGe solar cells. Similar to Chapter 2, the discussion follows a progression of an introduction followed by a brief literature review, followed by fabrication and measurement techniques. Section 3.5 discusses some of the defect density profile results obtained. Chapter 4 provides a brief summary of the work. The list of references follows Chapter 4. The final item is the Appendix which contains a published work on the defect and doping properties of nc-SiGe.

CHAPTER 2: HETEROJUNCTION WITH INTRINSIC THIN-LAYER (HIT) DEVICES

2.1 Introduction to HIT Devices

Heterojunction with Intrinsic Thin-layer (HIT) solar cells are an important development in the field of photovoltaic devices. The potential to achieve high efficiencies is one of the primary factors that is drawing interest in HIT technology. A record efficiency of 25.6% was recently reported for a p+/n/n+ HIT cell fabricated by Panasonic [8]. This is another exciting development in HIT, eclipsing a previous record that had stood since 1998 [9].

HIT cells have several other benefits in addition to efficiency. One advantage of the HIT process over conventional c-Si processes is the relatively low-temperature process used for HIT. While conventional c-Si solar cells are fabricated by thermal diffusion at temperatures around 1000°C, HIT cells can be fabricated at temperatures of less than 200°C. HIT has the added advantage of having a shorter fabrication time. Another benefit of HIT cells is their efficiency at hotter operating temperatures [10]. This is shown in Figure 2.1a. As a solar cell heats up during prolonged exposure to sunlight, the efficiency tends to drop. However, the efficiency of HIT cells does not decrease as rapidly as normal c-Si with increasing operating temperature. An additional advantage of HIT cells is their improved performance yield across the months of the year [10], as shown in Figure 2.1b. One other interesting benefit of HIT is that their symmetry lends the capability to fabricate bifacial modules, which achieve higher efficiency by taking advantage of light reflected from behind and entering the back of the wafer.

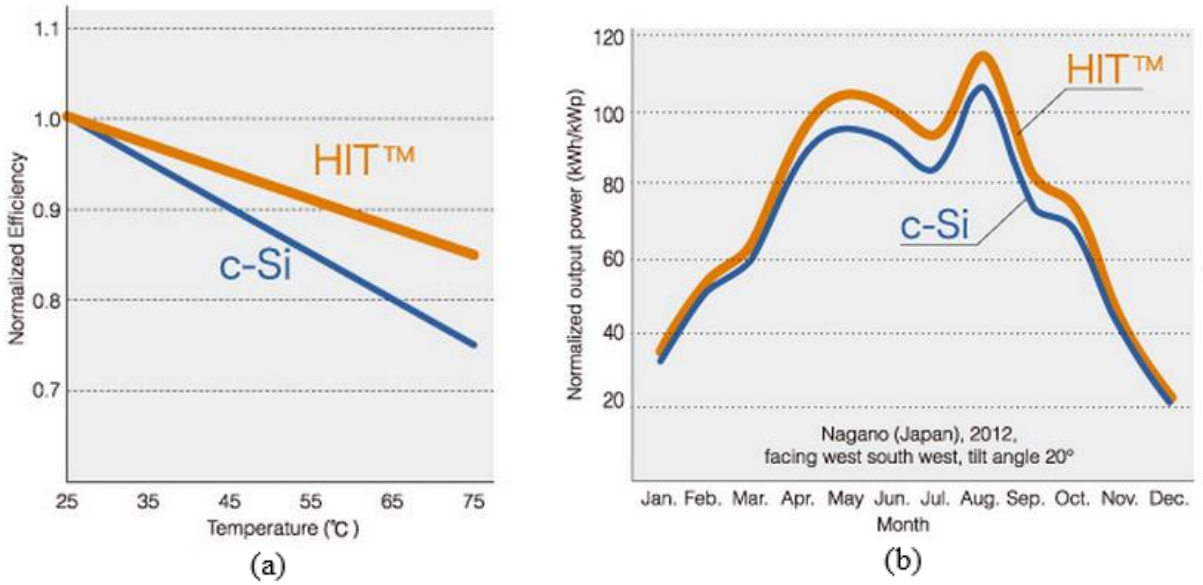

Figure 2.1 (a) Normalized efficiency of HIT and c-Si solar cells vs. temperature, (b) Normalized output power of HIT and c-Si solar cells vs. time of year [10]

All the prior work on HIT solar cells has used a p+/n/n+ structure. In this paper, we examine HIT solar cells that are fabricated using the opposite structure: n+/p/p+, where the substrate is a p-type c-Si wafer.

2.2 Literature Review

This section explores the literature related to the fabrication and characteristics of HIT solar cells.

2.2.1 Material Growth

While traditional c-Si cells use high-temperature diffusion of dopants to make a homojunction, HIT cells are fabricated by taking a c-Si wafer and depositing thin layers of a-Si on both sides of the wafer to create a heterojunction. In our process, a-Si:H layers are deposited using plasma enhanced chemical vapor deposition (PECVD). HIT cells use the large bandgap of a-Si:H as an emitter with the silicon wafer. The large band offset causes the carriers to move in only one direction. However, one must account for the dangling bonds on the

surface of the wafer which cause undesired recombination. HIT cells deal with this issue by containing an intrinsic layer (i-layer) of a-Si:H between the wafer and the a-Si:H emitter. This serves to reduce recombination losses by passivating the dangling bonds [11].

When growing silicon thin films in plasma, the growth depends on many factors such as the RF power, frequency, substrate temperature, gas pressure, gas composition, gas flow magnitude, and electrode geometry. It is important to understand the physics involved in the deposition. When performing PECVD to deposit a-Si, many radicals are produced, as the decomposition of silane (SiH_4) generates SiH_3, SiH_2, and SiH. While it was calculated by Kushner that SiH_2 and SiH_3 should be nearly equally generated [12], many experiments found that SiH_3 was the dominant radical responsible for the growth [13, 14]. However, experiments performed by Dalal indicate that the density of all three (SiH_3, SiH_2, SiH) coming through the substrate is about the same [15]. It was also demonstrated by Hamers et al. that ions account for a good percentage of the growth [16], contrary to a conventional assumption that the growth is only from radicals.

A standard growth model for a-Si:H was developed by Matsuda, Gallagher, and Perrin [17-19], sometimes called the MGP model. A diagram of the growth of a-Si:H is shown in Figure 2.2 [20]. In this model, the dangling bonds at the surface are almost all bonded with hydrogen, and occasionally a bond opens to insertion by a silyl (SiH_3) radical. However, this model does not consider the elimination of H from the surface, and is inadequate to explain many critical results.

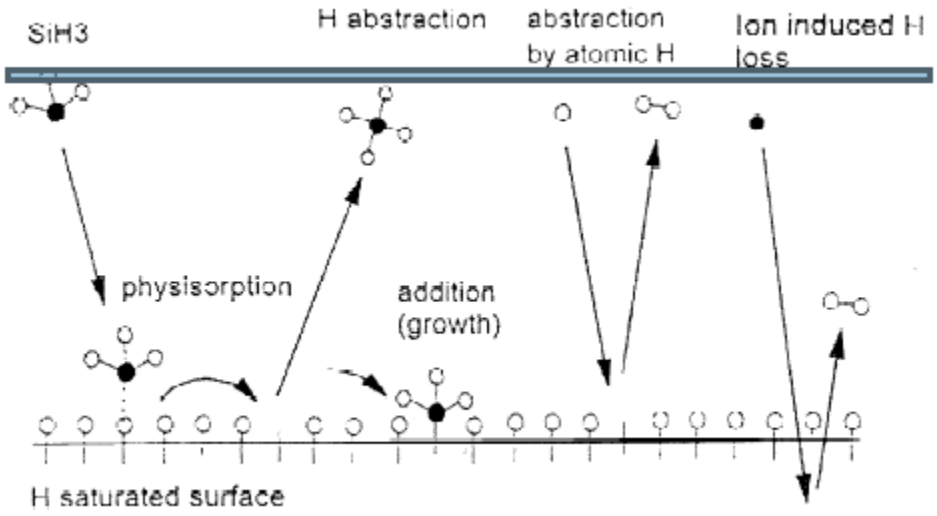

Figure 2.2 The standard model for the growth of a-Si [20]

It was stated by Matsuda [21], Gallagher [13], and Perrin et al. [22] that the growth of a-Si is primarily limited by the surface diffusion of radicals such as SiH_3. The radical bonds when it locates an open site. They theorized that the breaking of the Si-H bonds at the surface causes the elimination of H, and consequently, the neighboring H bonded to adjacent Si atoms become cross-linked. However, Dalal [23] explained that this theory was not thermodynamically likely, but rather that the elimination of the excess hydrogen is facilitated by both H ions and radicals, as well as bombardment with inert ions. He suggested that the primary factor in determining the growth of high quality a-Si films is not the surface diffusion, but the removal of the surface hydrogen; and that the hydrogen is not removed by reactions with neighboring hydrogen bonded to adjacent silicon atoms, but rather by extraction with H radicals and ions. This can be achieved with hydrogen dilution. Not only is H dilution responsible for removing H from the surface, but it also improves the radical selectivity in the growth process by increasing the fraction of silyl radicals [24]. On the other hand, in the absence of hydrogen ions, or with low ion energy, the material will contain a high amount of defects [25].

A study of the relationship between the RF power, hydrogen dilution, and other factors in PECVD deposition of a-Si:H is reported by Lien et al. [26]. In the silane plasma, most of the reactants dissociate into SiH_2, which has the lowest excitation energy. They state that the presence of the hydrogen along with the silane can help to generate SiH_3 radicals rather than SiH_2 which favors deposition of the thin Si film. The reactions involving the dissociation of SiH_3 in the plasma are detected in optical emission spectrometry (OES) as a feature around 400 nm. These features are present in Figure 2.3a, which shows the OES spectra of pure SiH_4 RF plasma discharges with various powers. Figure 2.3b summarizes the effects of the excited radical intensity and the deposition rate versus the RF power.

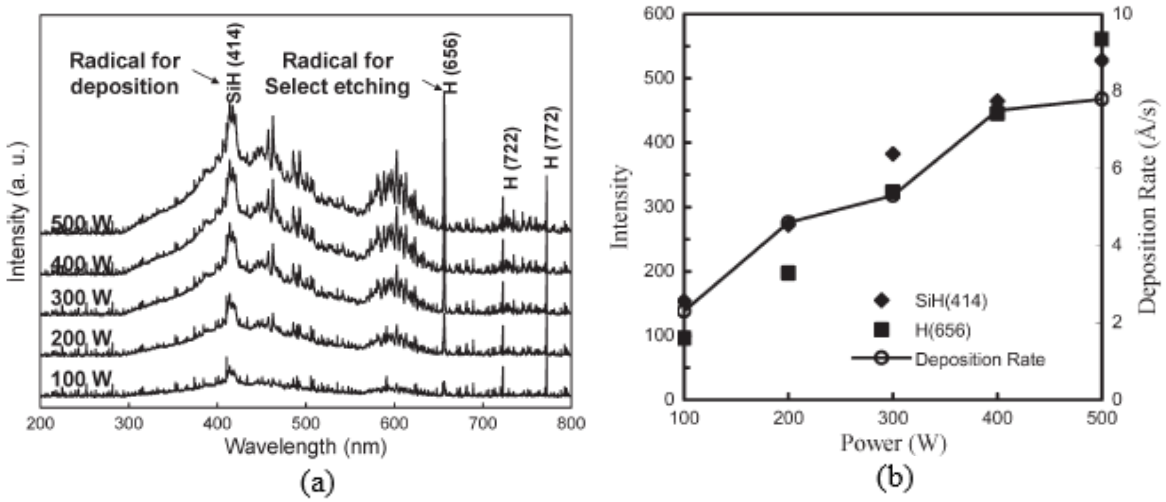

Figure 2.3 (a) Optical emission spectra of plasma states with different RF powers, (b) Results of the radical intensity and deposition rate as a function of different RF powers from 100 to 500 W [26]

The optical emission spectra in Figure 2.4a show the effects of changing the hydrogen dilution on the radical intensity and deposition rate, summarized in Figure 2.4b. As the hydrogen dilution increases, the number of excited SiH radicals is noticeably reduced, which lowers the deposition rate. It was also observed that while the intensity of SiH was reduced, the intensity of H remained the same.

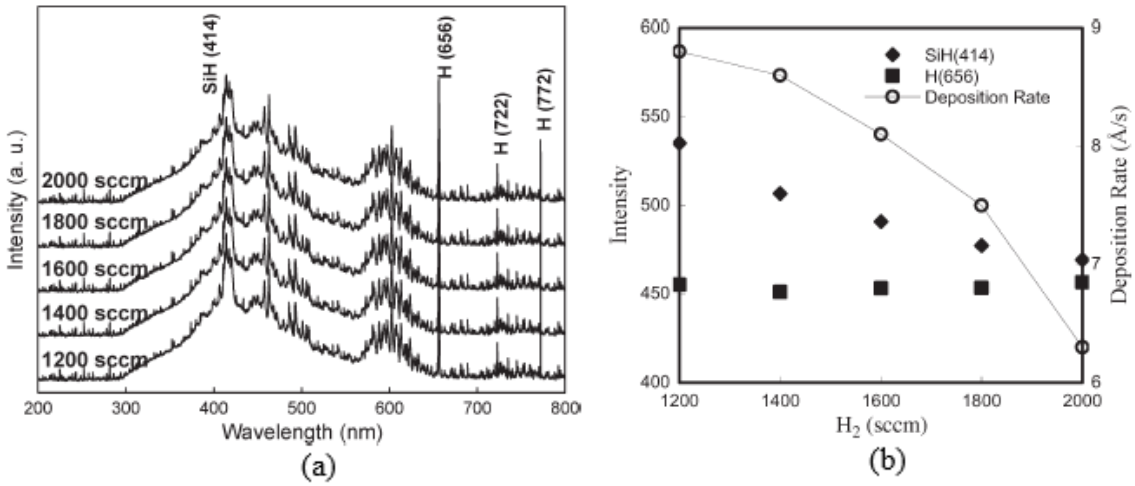

Figure 2.4 (a) Optical emission spectra of plasma states with different H_2 dilutions, (b) Results of the radical intensity and deposition rate as a function of H_2 dilution from 1200 to 2000 sccm [26]

A study of a-Si:H films by Kessels et al. reports on the relationship between the hydrogen content and the substrate temperature, for a variety of growth rates [27]. It was observed that for high growth rates, the substrate temperature had to be increased substantially to still obtain good quality films. This is shown in Figure 2.5.

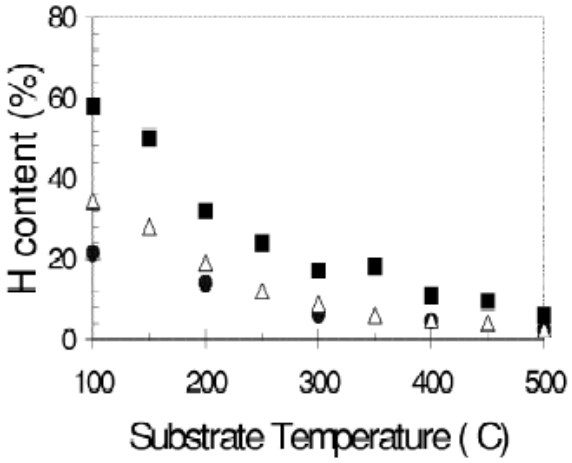

Figure 2.5 H content of ETP deposited a-Si:H films. The circles stand for films grown at a rate of 0.3 nm/s, triangles for 3 nm/s, and squares for 11 nm/s [28]

2.2.2 Device Performance

There are several important factors that affect the characteristics of HIT solar cells. One of the characteristics of most interest is the open-circuit voltage (V_{oc}). In order to achieve high open-circuit voltage, one must effectively passivate the defects on the c-Si surface. This means that the intrinsic a-Si:H layer must be of high quality. Tanaka et al. explained that a high V_{oc} cannot be achieved in basic heterojunction cells without the intrinsic layers, due to tunneling caused by the many localized states in the doped layer [29]. Furthermore, the insertion of the intrinsic a-Si:H layer onto the back surface functions to increase the open-circuit voltage by reducing the recombination velocity of the interface in the back surface field (BSF) structure [30].

A study involving the thickness of doped a-Si layers was carried out by Wakisaka et al. [31]. They found that the open-circuit voltage of a HIT solar cell does not depend on the thickness of the a-Si film, but the short-circuit current decreases with thicker films, as demonstrated in Figure 2.6. They explain this to be due to increasing optical absorption in the a-Si layer which does not contribute to the power generation. There is a gradual decline in total efficiency as the thickness increases.

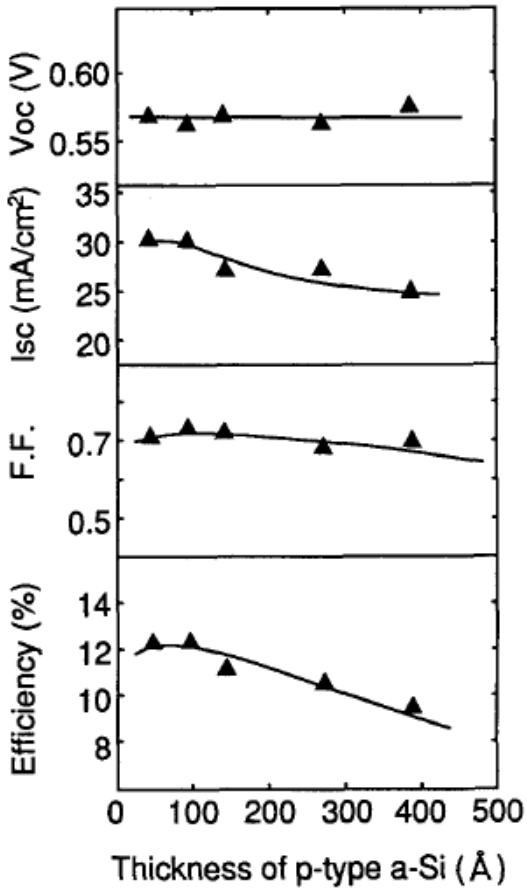

Figure 2.6 Output characteristics of p-type a-Si / n-type c-Si heterojunction solar cells as functions of p-type a-Si film thickness (c-Si: 0.65-0.75 Ω-cm) [31]

Wakisaka, Taguchi, and Sawada also investigated the effects of changing the thickness of the intrinsic a-Si layer [31], shown in Figure 2.7. They observed that both V_{oc} and FF were better than that of a simple heterojunction with no i-layer, up to a certain thickness. The results indicate that while the i-layer is necessary, it should not be too thick. For maximum efficiency, the plot shows that the optimum thickness of the a-Si i-layer should be about 50 Å (5 nm), which is the thickness we use in our own process.

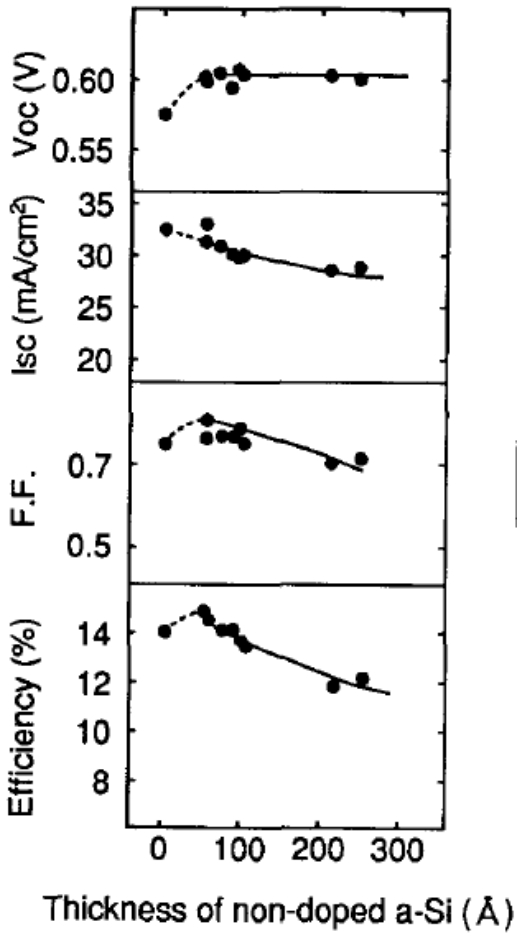

Figure 2.7 Output characteristics of the HIT structure solar cells as functions of the non-doped a-Si film thickness (c-Si: 1.35-2.25 Ω-cm) [31]

The c-Si wafer thickness is another factor that influences the electronic characteristics of HIT cells. Mishima et al. reported that the open-circuit voltage and short-circuit current (I_{sc}) were affected in different ways by changing the wafer thickness [32]. They found that the I_{sc} decreased for thinner cells, while V_{oc} increased with cell thinning, shown in Figure 2.8. They explained these phenomena by pointing out that the total recombination velocity was only determined by the bulk recombination, due to the low surface recombination velocity of HIT solar cells [33]. For this reason, they were able to maintain high efficiency even for cell thicknesses below 100 μm.

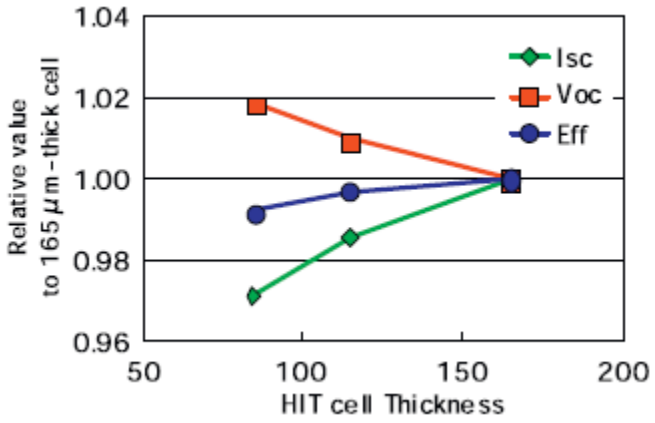

Figure 2.8 Thickness dependence of HIT (I_{sc}, V_{oc}, Efficiency) [32]

2.3 Fabrication Process

In this section, the processes used in fabrication of HIT solar cells are explained. Many of the procedures discussed are similar for nc-Si and nc-SiGe solar cells.

2.3.1 Plasma Enhanced Chemical Vapor Deposition (PECVD)

PECVD is a commonly used process for deposition of thin films in silicon-based solar cells. The primary advantage of PECVD over standard CVD is the capability to deposit films at lower temperatures. The benefits of using high frequency instead of DC plasma were first shown by Robertson [34]. High frequency plasma contains higher electron density and lower ion energy. Electron density is higher with increasing frequency, leading to a higher rate of deposition. Ion energy is lower with increasing frequency, which helps to make films of a better quality. Figure 2.9 demonstrates that the defect formation threshold is about 50 MHz; at this frequency, we can obtain higher electron density.

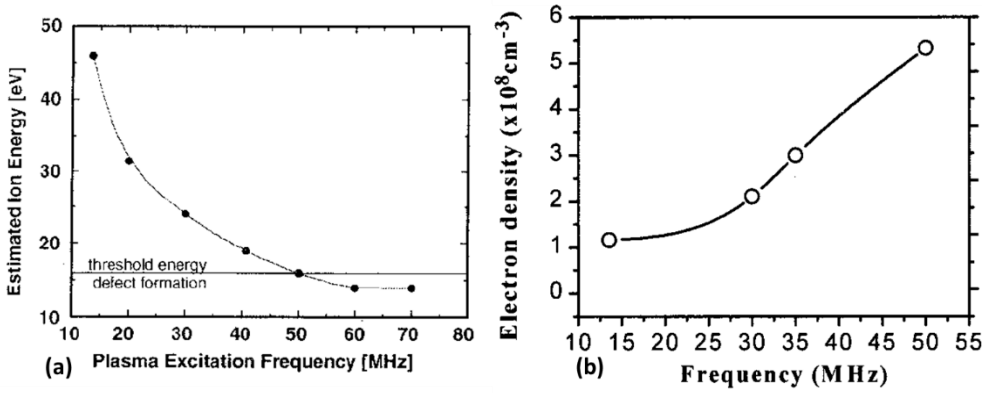

Figure 2.9 Variation of plasma parameters with an increase in plasma frequency (a) Ion energy vs. Frequency [35] (b) Electron density vs. Frequency [36]

The four main sections of a PECVD system are the reaction chamber, the power supply, the plasma monitoring networks, and the vacuum pump. Figure 2.10 shows the schematic diagram of a typical PECVD system. Inside the reaction chamber, an electrode and the substrate holder act as a parallel plate capacitor. The chamber connects to the gas manifold, vacuum system, power generator, and plasma monitoring equipment. The gases are all hooked up to the gas manifold by a series of valves and mass flow controllers that regulate the flow of gas into the reaction chamber. In the vacuum system, the roughing pump takes the pressure from atmosphere to less than 1 torr, and the turbo pump is responsible for pumping down to lower pressures around 10^{-7} torr. The plasma is created using RF power from a function generator connected to a power amplifier, which is hooked up to an impedance matching box in order to obtain maximum forward power. The plasma characteristics are monitored using an oscilloscope and multimeter. A baratron is used to continuously monitor the pressure, and a thermocouple is used to track the temperature.

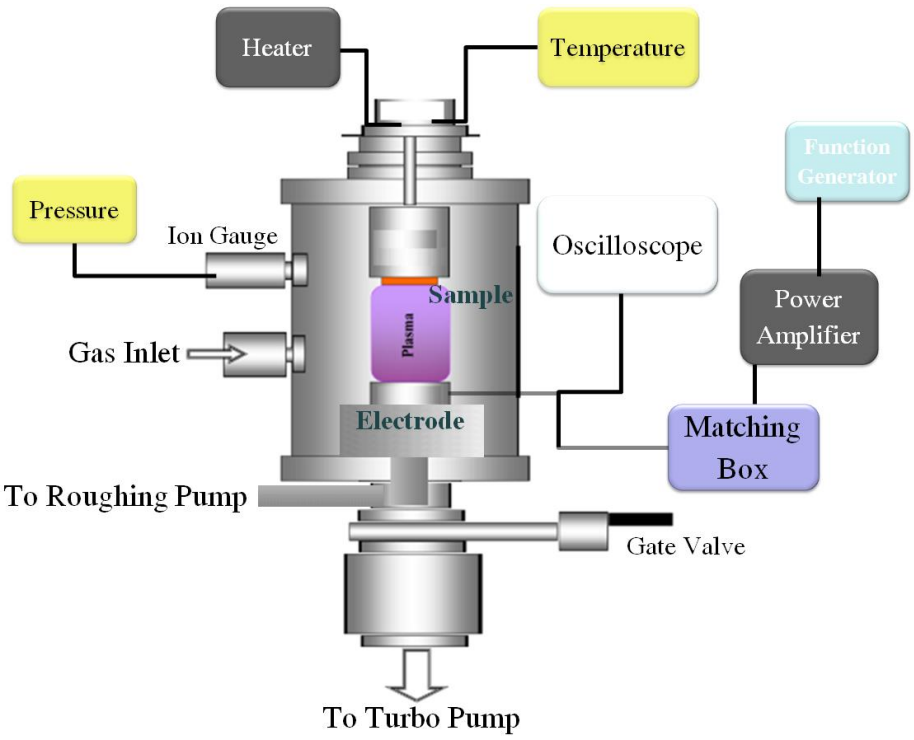

Figure 2.10 Schematic diagram of PECVD reactor [37]

Amorphous and nanocrystalline films can be grown with a high frequency capacitively coupled RF plasma (approx. 45 MHz). Silicon (and/or germanium) is deposited from its gaseous phase into a solid phase on the substrate. Two PECVD reactors at the Iowa State University Microelectronics Research Center were used for thin film deposition: Reactor 1 (R1) and Reactor 2 (R2). The reactors are pictured in Figure 2.11. For the HIT samples, all the layers were deposited in R2. For the nanocrystalline samples, R1 was primarily used for the intrinsic layer (to avoid contamination from dopant gases), and R2 was used for the doped layers. In between runs, the chambers were cleansed with an oxygen plasma to help remove contaminants deposited on the chamber walls.

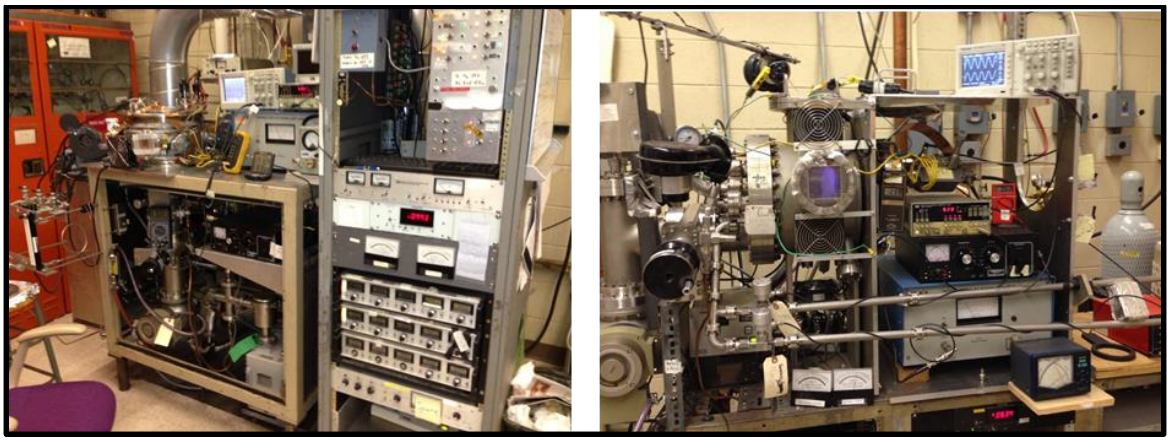

Figure 2.11 PECVD reactors at Iowa State University, R1 (left) and R2 (right)

2.3.2 Sample Preparation and Deposition

The n+/p/p+ HIT solar cells use a bare p-type silicon wafer as the starting substrate. The substrates are pre-cleaned to remove unwanted impurities on the surface using the following steps: boiling in acetone, followed by boiling in a solution of ammonium hydroxide (NH_4OH) and hydrogen peroxide (H_2O_2), followed by ultrasonication in methanol. At the conclusion of the cleaning, the substrates are loaded into the reactor. Once a substrate is loaded into the reaction chamber, we perform several purges with nitrogen, followed by pressurized evacuation purges using hydrogen and silane, to help ensure that the system is free of oxygen and moisture. When the pressure in the chamber reaches the low microtorr range, then we start a dummy plasma layer (with the shutter closed) in order to coat the inside of the chamber and to obtain a stable plasma, while the substrate is being brought up to the desired temperature.

The deposition begins on the back side of the wafer. The first layer is a 5 nm thick a-Si intrinsic layer. The next layer is a 40 nm thick a-Si p+ layer, doped using diborane. The p+ layer is heavily doped to ensure good ohmic contact on the back contact. After the p+ layer is finished, the wafer is removed and the reactor chamber is plasma cleaned with oxygen to remove the influence of diborane from the chamber. Then the deposition continues on the top

(polished) side of the wafer. Same as with the back side, the first layer is a 5 nm thick a-Si intrinsic layer. After this, a 20 nm thick a-Si n+ layer is deposited, doped using phosphine. The basic device structure of the n+/p/p+ HIT solar cell is shown in Figure 2.12a (layers not to scale). The band diagram of the n+/p/p+ HIT solar cell is shown in Figure 2.12b.

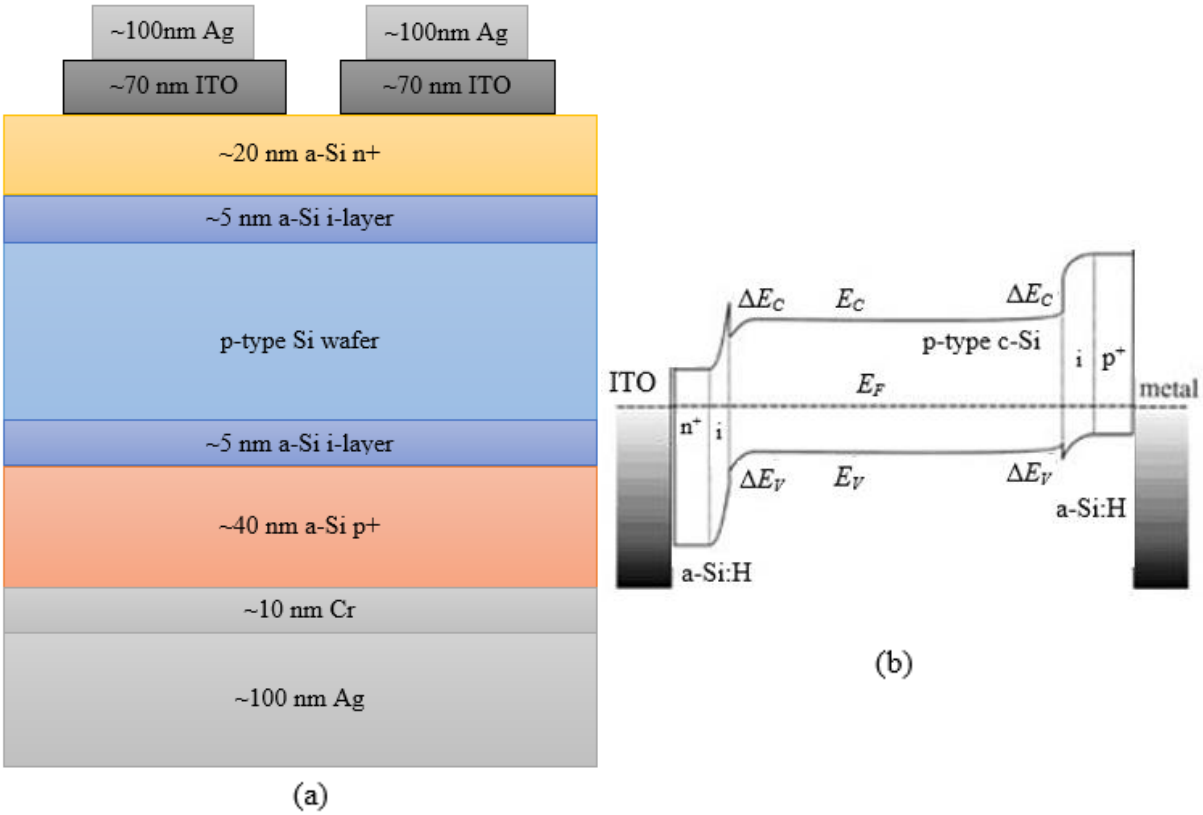

Figure 2.12 (a) Device structure and (b) band diagram of n+/p/p+ HIT solar cell

To make the top contact, a transparent conductive oxide such as indium tin oxide is deposited using a sputtering system. The top and bottom contacts are completed by evaporation of metal. These topics are covered in the following sections.

2.3.3 Sputtering

Sputtering is a commonly used process for deposition of transparent conductive oxides in the semiconductor industry, due to being typically faster and simpler than thermal or other evaporation. Indium tin oxide (ITO) is used as the top contact for our HIT and nanocrystalline

solar cells. In the sputtering process, a target material is bombarded with high energy argon ions. The argon ions knock the material off the target and the material is deposited on the substrate. To get better quality films and higher deposition rates, an RF plasma is used. Figure 2.13 shows a schematic diagram of the custom in-house built RF sputtering system used for depositing ITO on our samples.

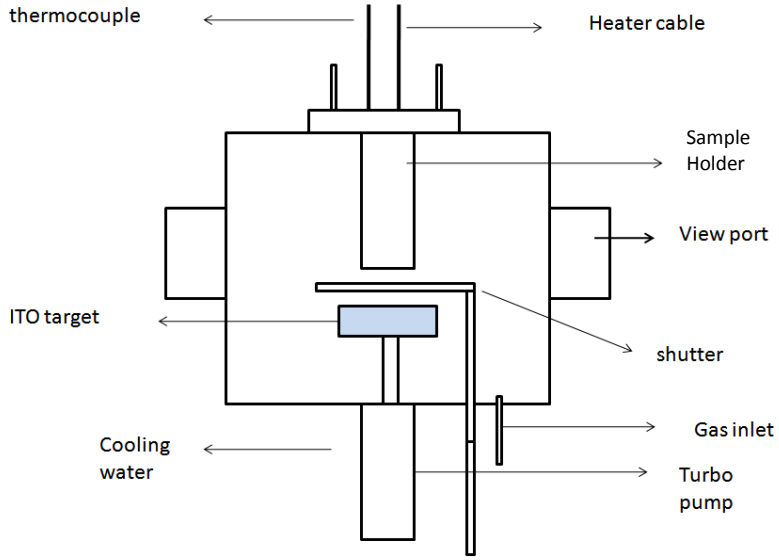

Figure 2.13 Schematic diagram of RF sputtering system [37]

To calibrate the growth rate of ITO, we deposit thick films of ITO on Corning 7059 glass slides and measure the thickness (using optical transmission measurement) and resistivity. For the HIT cells, the ITO was deposited at 150°C and 5 mT, and the resistivity was measured to be about 4×10^{-4}. For the nanocrystalline cells, the ITO was deposited at 225°C and 5 mT, and the resistivity was observed to be about 3×10^{-4} ohm-cm. For the working wavelengths, transmission exceeding 80% was observed. To obtain the best antireflection coating, the wavelength where maximum absorption occurs is used to calculate the thickness needed, and consequently, we typically deposited the ITO at a thickness of 70 nm.

2.3.4 Evaporation

Evaporation is a useful technique for deposition of thin metal layers to make contacts. In electron beam evaporation, the target material is bombarded with an electron beam to transform the atoms into their gaseous phase. The beam originates from a tungsten filament under high vacuum. The atoms move across the chamber and precipitate into their solid form to coat the sample with a thin layer of the target material. The vacuum system works similar to the vacuum system used in a PECVD reactor. A roughing pump evacuates the chamber initially, and a turbo pump brings the pressure down to the 10^{-5} or 10^{-6} torr range. A rotating substrate holder ensures even deposition of the metal. A diagram of the electron beam evaporation system is shown in Figure 2.14.

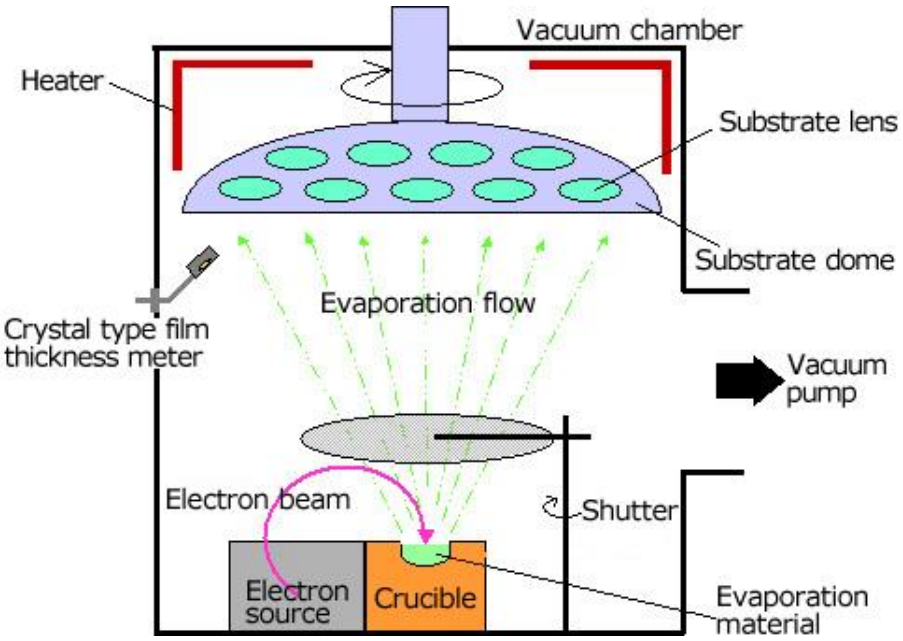

Figure 2.14 Schematic diagram of electron beam evaporator [38]

To deposit the metal contacts for our HIT cells, chromium and silver are evaporated onto the back side of the wafer to make the bottom contact. A 10 nm layer of chromium is first evaporated to promote adhesion of the silver, after which a 100 nm layer of silver is evaporated.

Then, for some samples, we evaporate a small 3 mm × 1 mm silver bar on top of the ITO to improve the top contact and increase the fill factor.

2.3.5 Mesa Etching

Mesa etching is a well-known technique in the semiconductor industry for etching silicon. The size of the amorphous layers deposited on the wafer is about 2.5 cm × 2.5 cm. However, the ITO contact has a smaller area, from 0.125 to 0.25 cm^2 (depending on the mask used). This leads to undesired shunt current and capacitance fringing effects. Since it is important to have a well-defined area, the remaining non-contact silicon needs to be etched away, via mesa etching. The two primary ingredients are nitric acid and hydrofluoric acid, used as an oxidizer and an oxide etcher, respectively. The contacts on the sample are first masked, by heating and applying black wax. When the sample cools, it is etched in the solution of nitric acid, hydrofluoric acid, and water (10:3:5 ratio) for 20-30 seconds. The exposed silicon is oxidized by the nitric acid and etched away by the hydrofluoric acid. After etching is complete, the device is rinsed and the black wax is removed, leaving the device ready for characterization.

2.4 Measurement Techniques

The fundamental characteristics of solar cells can be determined using many different electrical and optical measurement techniques. The characterization of parameters is a vital facet of research that helps us to proceed in the right direction. It is important to understand the electronic properties of devices and the structural properties of thin films. This section covers the characterization techniques for HIT solar cells and some of the characterization techniques for nanocrystalline solar cells. These measurements were used on either HIT or both HIT and nanocrystalline samples; the additional measurements that were only performed on the nanocrystalline samples are discussed in Section 3.4.

2.4.1 Current-Voltage (IV) Measurements

The measurement of current as a function of voltage (IV) is the single most valuable tool for characterization of a solar cell. The IV measurement is used in determining the power conversion efficiency (PCE). Figure 2.15 shows a typical IV curve of a solar cell under illumination. From an IV curve, we obtain the open-circuit voltage (V_{oc}), the short-circuit current (J_{sc}), and the fill factor (FF). The curve crosses the x-axis at the open-circuit voltage, and crosses the y-axis at the short-circuit current.

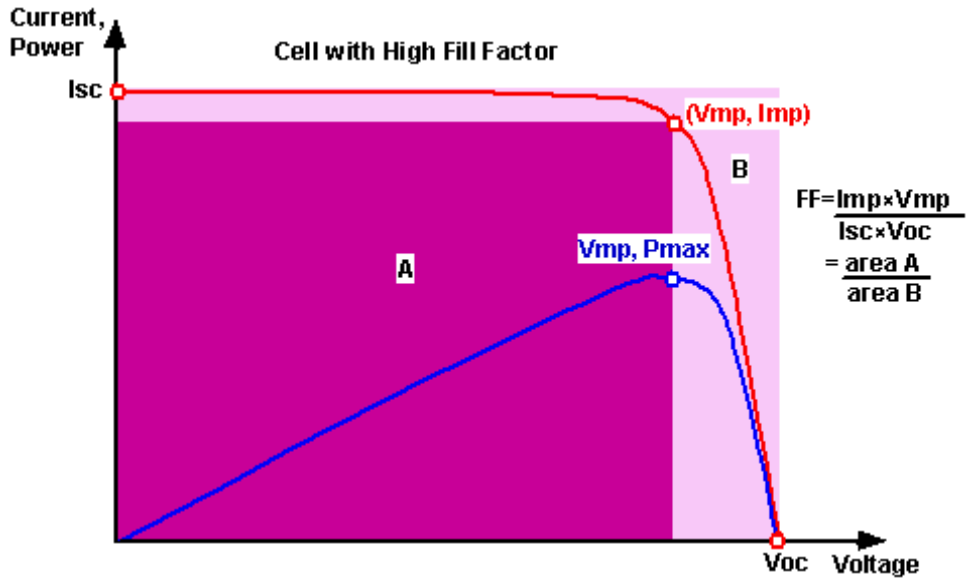

Figure 2.15 IV curve of a typical solar cell, also showing power [39]

The open-circuit voltage is the voltage across the cell when no current is flowing. The theoretical open-circuit voltage can be found using the formula:

$$V_{oc} = \frac{nkT}{q} \ln\left(\frac{J_{sc}}{J_0} + 1\right)$$

where n is the ideality factor, k is Boltzmann's constant, T is temperature, q is the charge of an electron, J_{sc} is the short circuit current density, and J_0 is the reverse saturation current density. In HIT solar cells, V_{oc} depends largely upon the doping of the wafer. In nanocrystalline solar

cells, V_{oc} is determined primarily by the i-layer crystallinity and by the interfaces present in the device, which help to control the reverse saturation current (J_0) [40].

The short-circuit current is the current generated by the solar cell when the load is shorted. The current flowing in a solar cell follows the equation:

$$J = J_L - J_0\left[\exp\left(\frac{qV}{nkT}\right) - 1\right]$$

where J_L is the light-generated current and V is the voltage. For nanocrystalline solar cells, J_{sc} depends upon the quality, thickness, and crystallinity of the intrinsic layer.

The fill factor is a measure of the "squareness" of the IV curve. FF is defined as the ratio of the maximum power point (V_{mp}. J_{mp}) to the ideal point (V_{oc}, J_{sc}), where V_{mp} and J_{mp} are the voltage and current at maximum power point, respectively. In equation form, it reads:

$$FF = \frac{J_{mp}V_{mp}}{J_{sc}V_{oc}}$$

FF is determined by the series resistance R_s, the shunt resistance R_{sh}, and the collection properties of the solar cell. For a good solar cell, we want the series resistance to be low and the shunt resistance to be high. If the series resistance is too high, there will be I^2R power loss. If the shunt resistance is too low, then current will leak and avoid going through the load, lowering the open-circuit voltage. These relationships are apparent by looking at Figure 2.16, which shows the equivalent circuit of a solar cell.

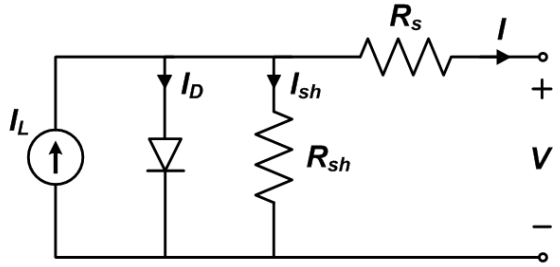

Figure 2.16 Electrical equivalent circuit of a solar cell [41]

The total power conversion efficiency (PCE), or simply efficiency, of a solar cell is given by the following equation:

$$Efficiency, PCE = \frac{J_{mp}V_{mp}}{P_{inc}} = \frac{FFJ_{sc}V_{oc}}{P_{inc}}$$

where P_{inc} is the power incident on the cell.

2.4.2 Quantum Efficiency (QE) Measurements

The Quantum Efficiency (QE) measurement explores the performance of a solar cell at different wavelengths across the solar spectrum. The external quantum efficiency (EQE) is defined as the ratio of the collected carriers to the incident photons per unit area per unit time. The internal quantum efficiency (IQE) is defined as the ratio of the collected carriers to the photons absorbed per unit area per unit time. In general, we measure the EQE spectrum and use it to calculate the IQE spectrum. Figure 2.17 shows the external quantum efficiency curve of a typical solar cell.

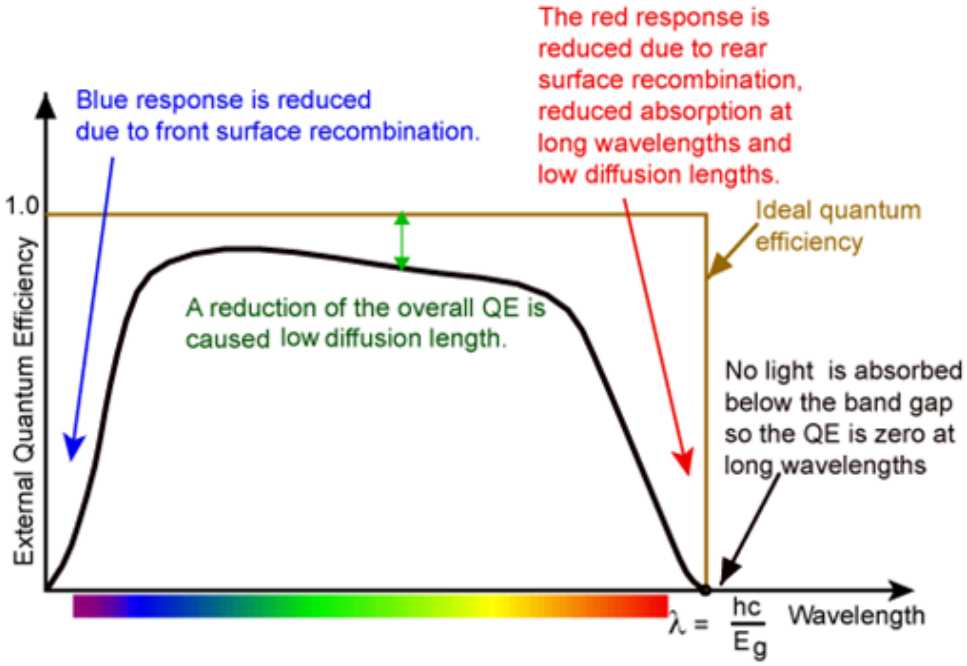

Figure 2.17 EQE curve of a solar cell [42]

The shorter wavelengths present in the solar irradiation spectrum, having a higher absorption coefficient, will get absorbed within the first few hundred nanometers, and the longer wavelengths will penetrate more deeply, and generate carriers within the intrinsic layer. For nanocrystalline solar cells, the QE is measured both at zero bias and -1 V bias. Application of a negative bias improves the electric field to obtain better carrier collection. If the ratio of the biased QE to unbiased QE is high at longer wavelengths, this is indicative of poor material properties in the i-layer in an n-i-p solar cell. Conversely, if the ratio is high at shorter wavelengths, this informs us of a poor interface between the p-layer and the i-layer [43].

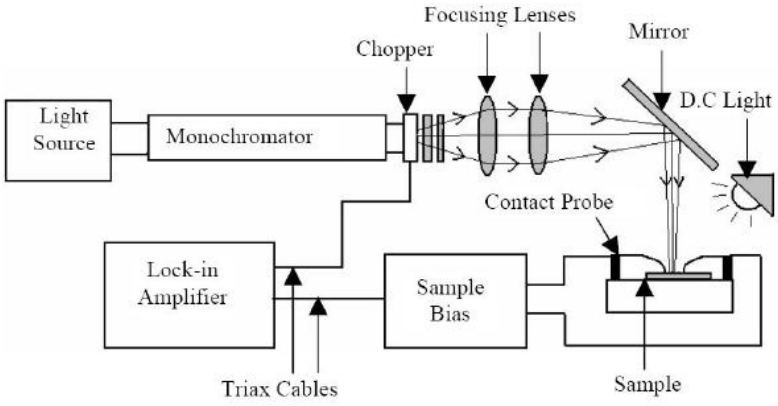

Figure 2.18 Schematic diagram of quantum efficiency measurement setup [37]

The schematic diagram of the QE measurement setup is shown in Figure 2.18. The light originates from a monochromator, which utilizes a type of grating structure to provide light of various particular wavelengths. The monochromatic beam passes through a light chopper with a rotational frequency of 13 Hz, yielding an AC beam. The beam is then directed through the focusing lenses and several optical filters, used at 580 nm, 700 nm, and 900 nm. The filters help to decrease the noise from lower harmonics. Finally, the beam reflects off a mirror tilted at a 45° angle to land on the sample.

When the light hits the sample, it generates a current which is converted to a voltage signal. This signal is connected to a lock-in amplifier which is set to amplify a frequency of 13 Hz, helping to elevate the desired signal above the surrounding noise and thus increasing the signal-to-noise ratio. Often the samples are also illuminated under a DC light source, helping to fill the midgap states with photogenerated carriers, and pinning the quasi-Fermi energy levels. During measurement, the received signal is recorded at each wavelength. For HIT solar cells, the wavelength is usually swept in steps of 20 nm from 400 to 1100 nm. In the case of nanocrystalline solar cells, the wavelength is generally swept from 400 to 900 nm.

To determine QE, the spectral response from the sample is compared with the spectral response of a reference photodiode. For a reference, we measure a standard silicon photodiode with a known QE response. The QE can then be determined from the equation:

$$QE_{cell} = QE_{ref} \frac{A_{ref}}{A_{cell}} \frac{V_{cell}}{V_{ref}}$$

where V_{ref} and V_{cell} are the signals from the reference cell and the sample, and A_{ref} and A_{cell} are the area of the reference cell and the sample, respectively. To find the integrated current from QE, we can use the formula:

$$J_{sc} = \sum q.\phi.QE$$

where q is the charge of an electron and ϕ is the photon flux per unit area, per unit time, per unit wavelength interval, in our case 20 nm. This integrated current density from QE is compared with the current density from the IV measurement, and the two should be a close match.

2.4.3 Capacitance-Voltage (CV) Measurements

The measurement of capacitance as a function of voltage is an important tool used in determination of the dopant density and defect density in a material. The CV measurement was originally developed by L.C. Kimerling [44]. In p+n junctions where the traps are assumed to be evenly distributed throughout the i-layer, the capacitance is related to the number of trap states by the equation:

$$\frac{C}{A} = 1/2\left[\frac{2q\varepsilon}{V+V_D}N(W)\right]^{\frac{1}{2}}$$

where C is the capacitance, A is the contact area, V is the applied voltage, V_D is the diffusion voltage, q is the charge of an electron, ε is the dielectric constant of the material, and N(W) is the total space charge density at the edge of the depletion width. When we plot the square of the area divided by capacitance $(A/C)^2$ against the voltage, we obtain a straight line (at low bias) with a slope proportional to N(W). The space charge density is composed of the traps that are responding to our applied conditions such as the applied bias, measurement temperature, and AC frequency. At high reverse bias, both the shallow and deep states respond; however, at lower reverse bias, only the shallow states will respond. Using different frequencies, we can estimate either the deep traps or the shallow traps. Using low frequency CV measurement at 100 Hz in nanocrystalline samples, we can use the slope at low reverse bias (as mentioned above) to estimate the defect density of the material. An example of this is shown in Figure 2.19.

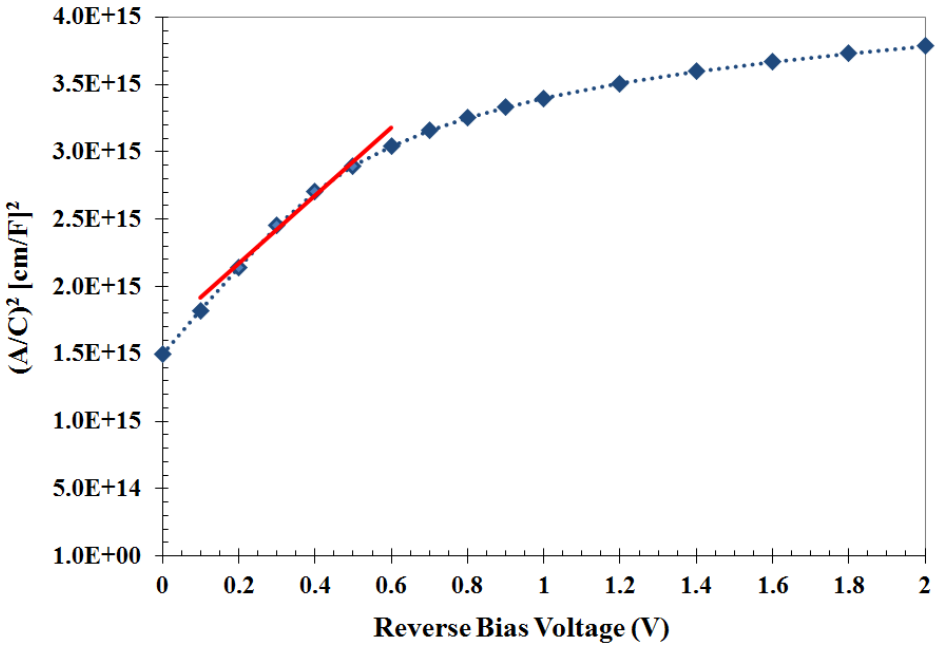

Figure 2.19 Low frequency CV measurement of a nc-Si:H solar cell

Using high frequency CV measurement at 100 kHz, the thickness of the i-layer and the dopant density can be estimated. The depletion width increases with increasing reverse bias, and it saturates when the i-layer has become entirely depleted. The capacitance value after this point is known as the saturation capacitance and can be used to calculate the i-layer thickness by using the parallel plate capacitance equation:

$$t = \varepsilon A / C$$

where t is the thickness of the i-layer, ε is the dielectric constant of the material, A is the contact area, and C is the saturation capacitance. The slope of the line can be used to calculate the doping density of the material in a similar method as finding the defect density; since the frequency is high in this case, only the doped states near the band edge can respond. An example of the high frequency CV measurement in a typical HIT cell is shown in Figure 2.20.

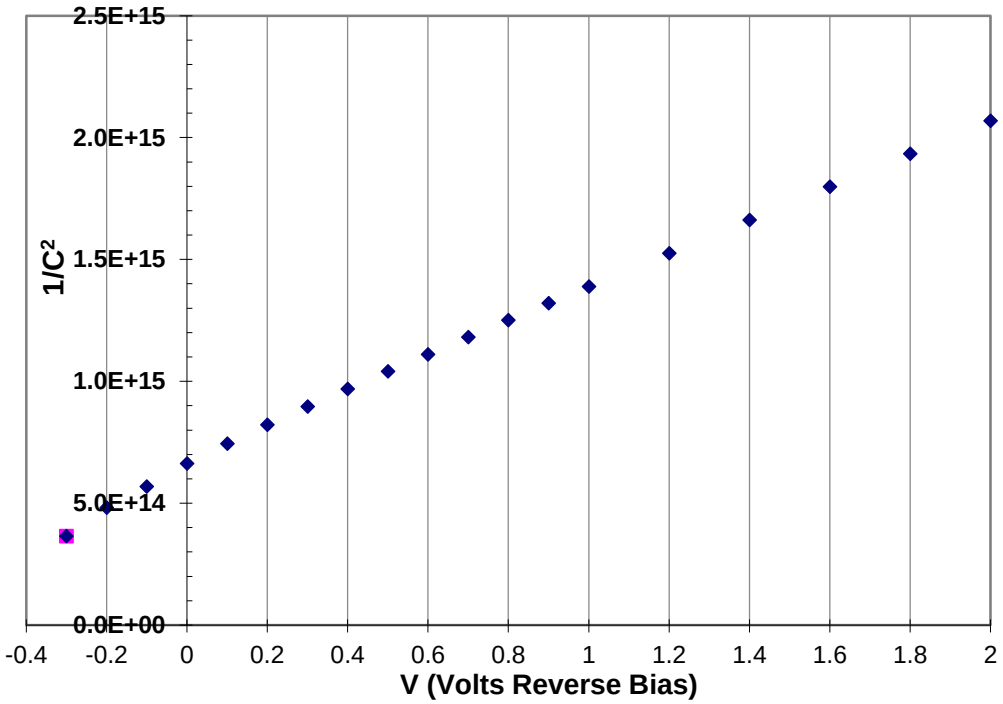

Figure 2.20 High frequency CV measurement of a HIT solar cell

2.4.4 Minority Carrier Lifetime Measurements

Carrier lifetime is an indicator of solar cell efficiency, and thus is an important consideration in choosing materials and doping levels for solar cells. If we increase the number of minority carriers above the equilibrium concentration, then the excess minority carriers will decay back down to the equilibrium level through recombination. The minority carrier lifetime of a semiconductor is defined as the average time that a generated charge carrier can remain in its excited state before it recombines. It is desirable for a solar cell to have a long minority carrier lifetime, as this increases the chance that the charge will avoid recombination and be available for collection.

The minority carrier lifetime of a solar cell can be determined using the reverse recovery technique, demonstrated by Kingston [45] and further explained by Streetman [46], where one observes the transient behavior as a junction is switched from forward to reverse

bias. The is an initial period of time, called the storage time, when the reverse current remains constant as the capacitive charge stored in the junction under forward bias is swept out of the depletion region. At the end of the storage time, the current decays exponentially to the steady-state reverse saturation current. Figure 2.21 shows some typical observed waveforms.

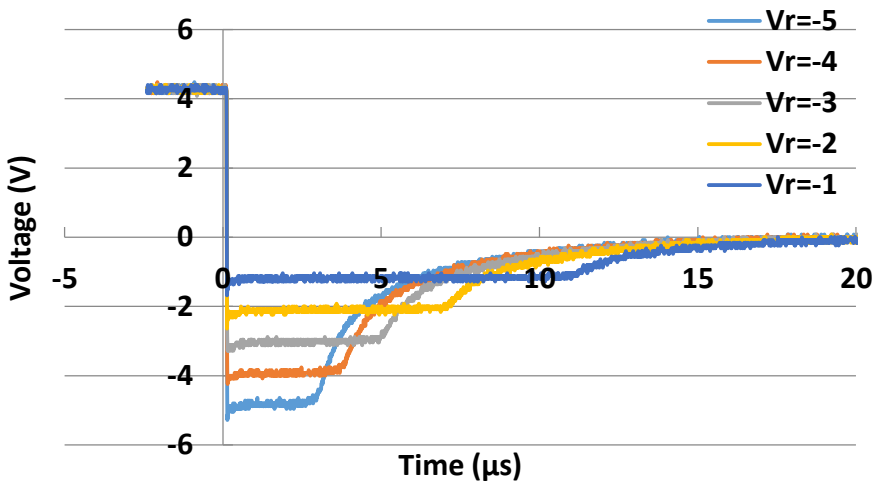

Figure 2.21 Storage time waveforms of a typical HIT solar cell (note that the legend shows the applied voltage, not the measured voltage)

The storage time is related to the average lifetime of the minority carriers [45, 46] by the equation:

$$\operatorname{erf}\left(\sqrt{\frac{t_s}{\tau_{p0}}}\right) = \frac{I_F}{I_F + I_R}$$

where t_s is the storage time, τ_{p0} is the minority carrier lifetime, and I_F and I_R are the forward and reverse currents, respectively. Rearranging the equation yields:

$$\tau_{p0} = \frac{t_s}{\left[\operatorname{erf}^{-1}\left(\frac{I_F}{I_F + I_R}\right)\right]^2}$$

The storage time is found by observing the point at which the current starts to decay back to the steady-state reverse saturation current. Since the resistance is constant, we can

alternatively substitute the ratio of voltages for the ratio of currents. When the measured storage times are plotted against the quantity of the inverse error function squared, then the slope of the resulting curve of storage times is the excess minority carrier lifetime. An example is shown in Figure 2.22.

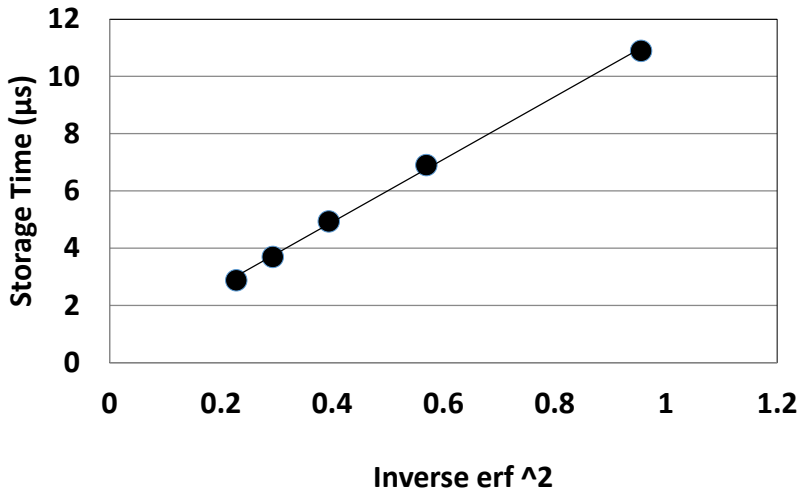

Figure 2.22 Plotting storage time vs. the erf quantity to find lifetime of a HIT cell

2.4.5 Diffusion Length Measurements

The minority carrier diffusion length of a solar cell is an important characteristic in determining the efficiency of the cell. The diffusion length is defined as the average length that a generated carrier moves before recombining. While Si wafers with high doping can have higher attainable open-circuit voltages, they also have greater recombination rates and thus have shorter diffusion lengths. If a material has a long diffusion length, this indicates a high carrier lifetime. The diffusion length is related to the carrier lifetime by the equation:

$$L = \sqrt{D\tau}$$

where L is the diffusion length, D is the diffusivity and τ is the lifetime. Alternatively, knowing the internal quantum efficiency (IQE) and the reflection and absorption spectrums of a solar

cell, the diffusion length can be calculated. The IQE is determined from the measured external quantum efficiency (EQE) by the relation:

$$IQE = \frac{EQE}{1 - R - T}$$

where R is the proportion of reflected light and T is the proportion of transmitted light. The reflection is measured using a spectrometer, and the transmission is zero due to the opacity of the sample. The diffusion length is related to the IQE by the formula:

$$IQE = \frac{\alpha L}{1 + \alpha L}$$

where L is the diffusion length and α is the absorption coefficient. Rearranging the equation, we obtain:

$$\frac{1}{L} = \frac{\frac{1}{IQE} - 1}{\frac{1}{\alpha}}$$

Thus, the diffusion length can be found by plotting the inverse of the IQE at each wavelength against the inverse of the absorption coefficient at each wavelength. The resulting line will have an intercept of 1 and a slope that corresponds to the inverse of the diffusion length. An example of this is shown in Figure 2.23.

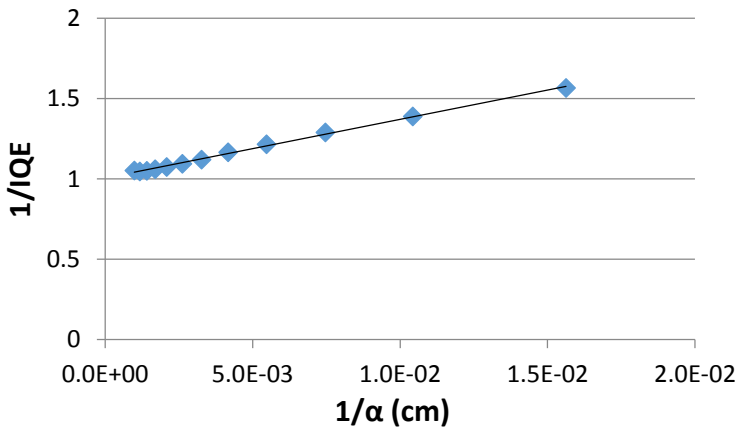

Figure 2.23 Inverse IQE plot to find lifetime of a typical HIT cell

2.5 Results

This chapter discusses the open-circuit voltage, lifetime, diffusion length, and other characteristics of n+/p/p+ HIT cells and their relationship to doping levels of the wafers used.

2.5.1 Measurements of an n+/p/p+ HIT Solar Cell

The following measurements were performed on a HIT solar cell with n+/p/p+ structure (made on a p-type Si wafer) with a doping level of approximately 4×10^{15} cm^{-3}. Its current-voltage (IV) characteristics are shown in Figure 2.24. The curve features an open-circuit voltage of 0.58 V and a reasonable fill factor of 71%.

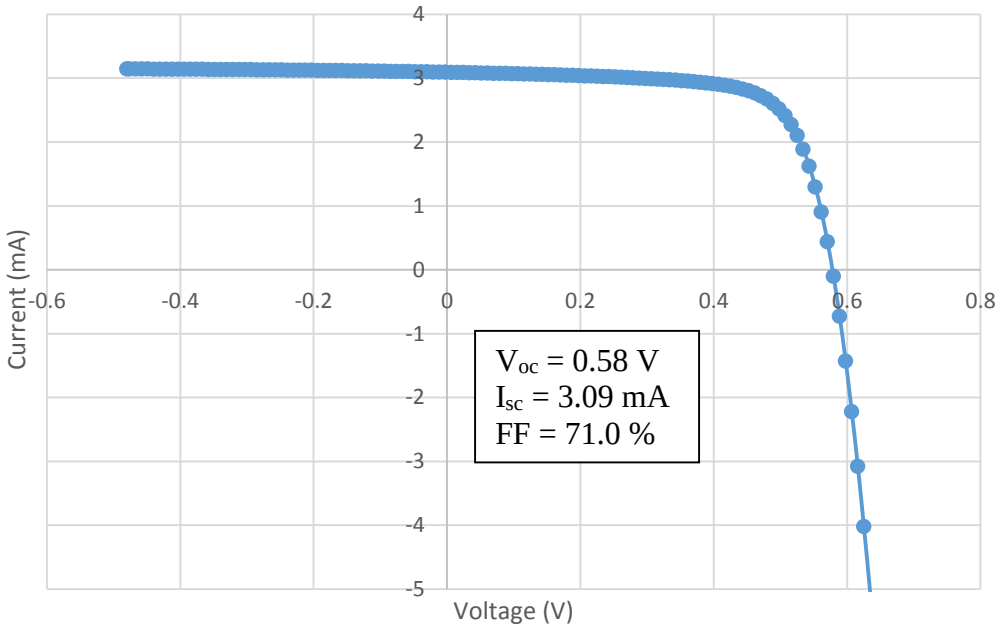

Figure 2.24 Measured IV curve of the HIT solar cell with wafer doping of 4×10^{15} cm^{-3}

The PCE of this cell was calculated to be about 12%. The quantum efficiency (QE) of the cell was measured from 400 to 1100 nm, pictured in Figure 2.25. The QE is smoothly distributed with suitable efficiency in the portions of the spectrum where solar irradiation occurs.

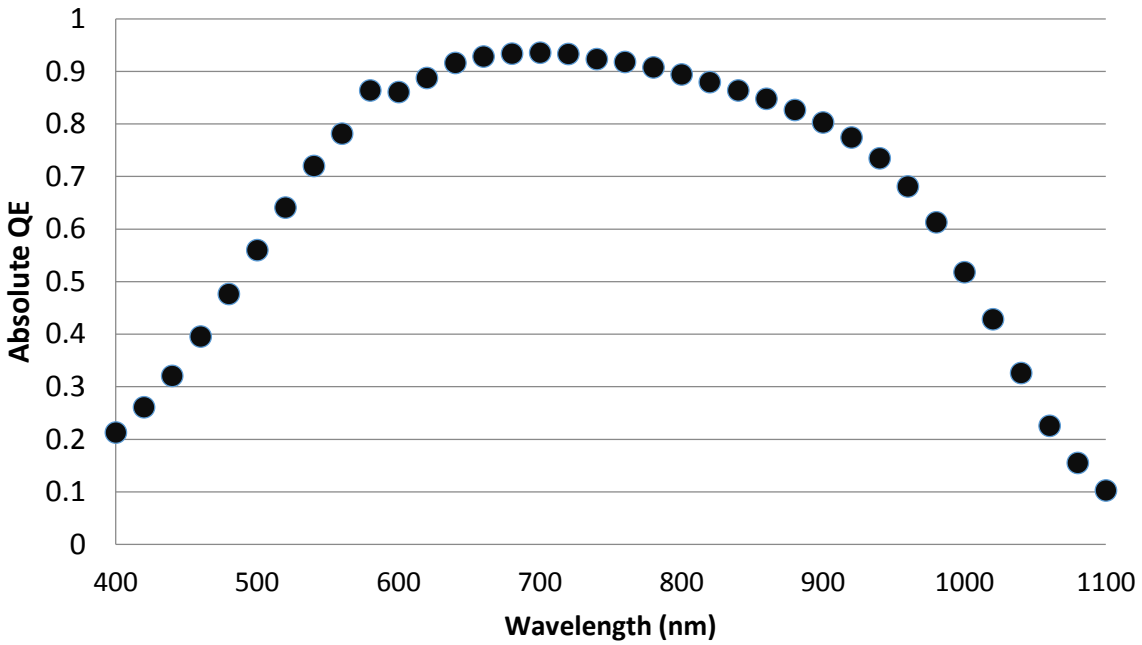

Figure 2.25 Measured QE spectrum of the HIT solar cell

The capacitance-voltage (CV) characteristics of the cell were measured at 100 kHz from -0.3 to 2.0 V reverse bias, with the resulting $1/C^2$ plot shown in Figure 2.26. Using the slope of the line, the dopant density is calculated to be about 5×10^{15} cm^{-3}, which is reasonably close to the nominal value of 4×10^{15} cm^{-3}.

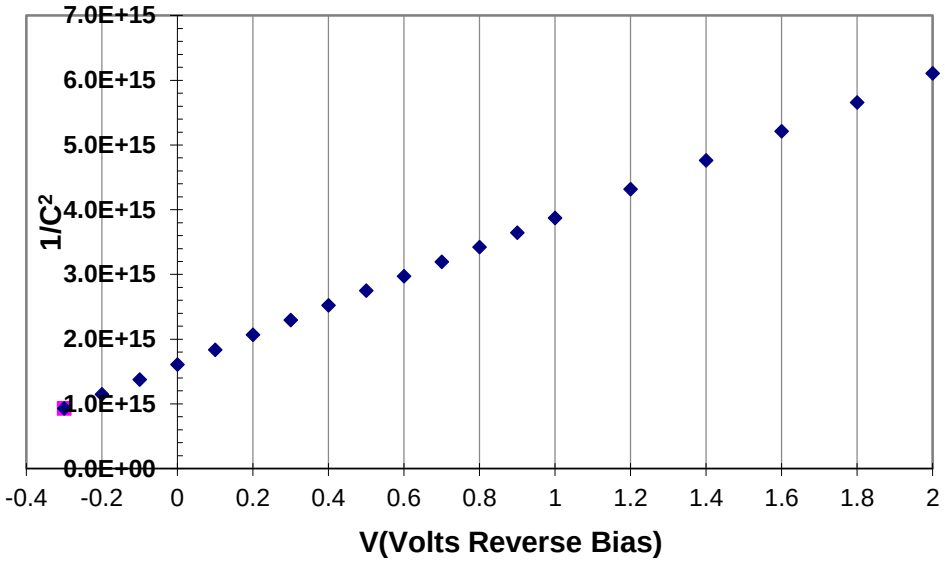

Figure 2.26 High frequency CV measurement of the HIT solar cell

The lifetime was measured using the reverse recovery method, as pictured in Figure 2.27, with the applied source voltages for each waveform listed in the legend.

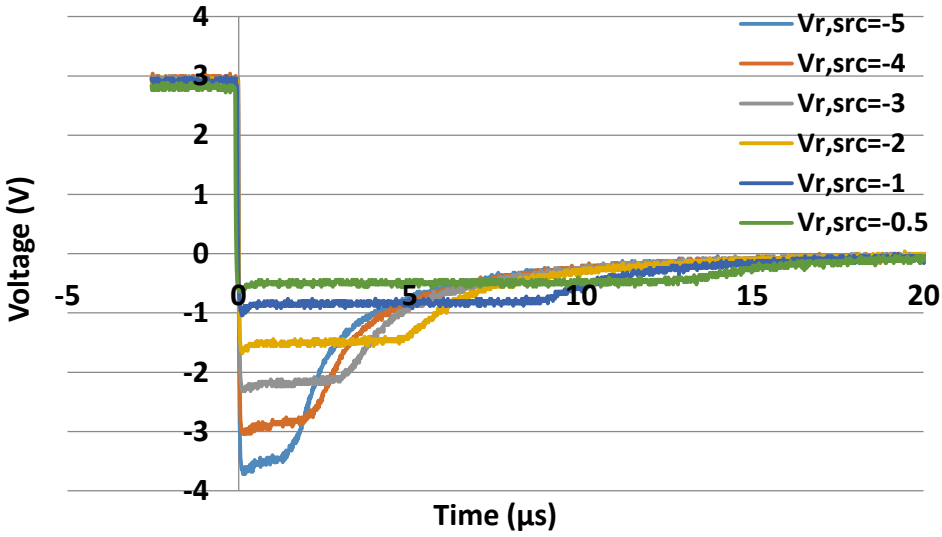

Figure 2.27 Measured storage time waveforms of the HIT solar cell

Each storage delay time is plotted in Figure 2.28 against the squared inverse error function term, according to the method described in Section 2.4.4. From the slope of the line, the lifetime is calculated to be approximately 13 µs.

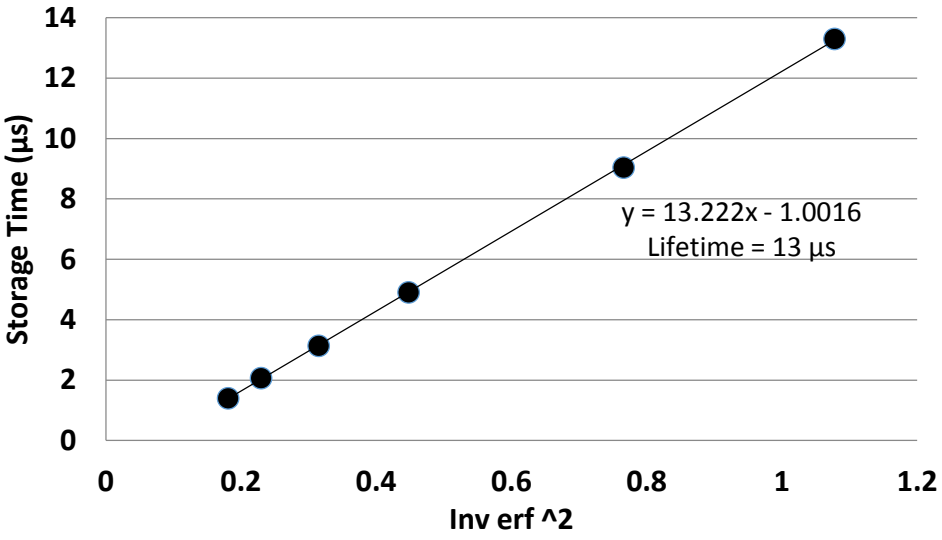

Figure 2.28 Storage times plotted to find the carrier lifetime of the HIT solar cell

The diffusion length was calculated using the method described in Section 2.4.5. After measuring the reflection spectrum to help calculate the IQE, then the inverse of IQE was plotted against the inverse of the absorption coefficient, shown in Figure 2.29. From the inverse of the slope of the line, the diffusion length is calculated to be approximately 175 µm.

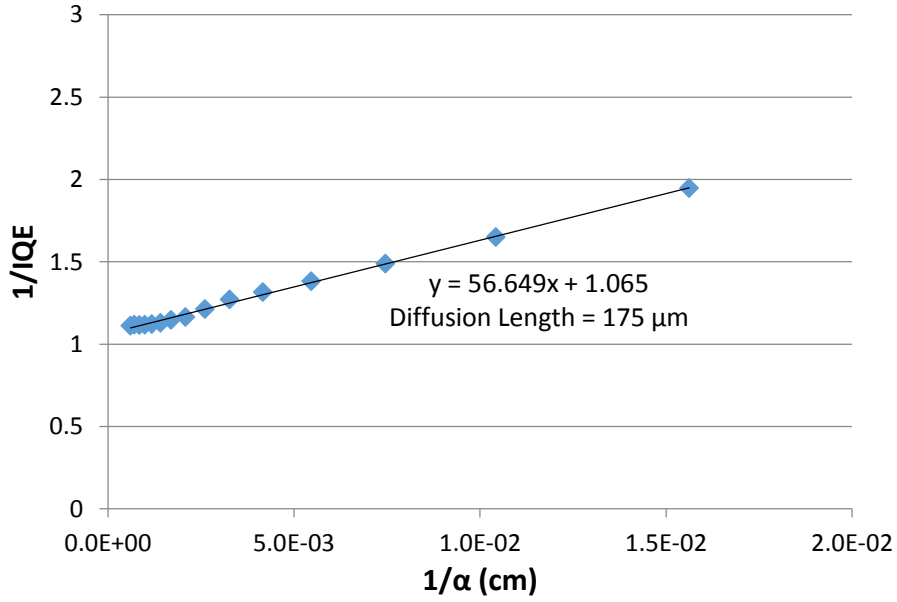

Figure 2.29 Inverse IQE plot to find the diffusion length of the HIT solar cell

2.5.2 Comparison of Characteristics with Wafer Doping Levels

In this section, the open-circuit voltage, minority carrier diffusion length, and other electronic characteristics are compared among several n+/p/p+ HIT cells using p-type wafers with different doping concentrations. The differences in open-circuit voltage are plotted in Figure 2.30. The V_{oc} is highest for the sample with intermediate doping concentration, while lower and higher doping concentrations have a lower V_{oc}.

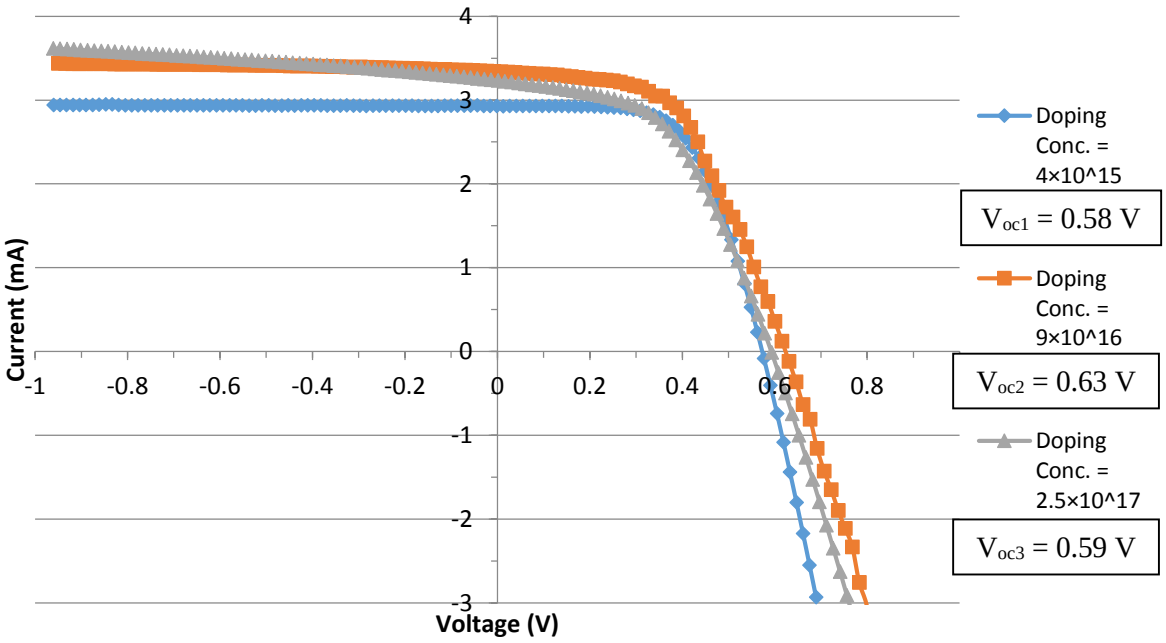

Figure 2.30 IV curves for HIT solar cells on wafers with different doping concentrations

The open-circuit voltage increases with doping up to a certain point until recombination losses cause it to decrease again. V_{oc} is the voltage where the forward bias diffusion current is the same as I_{sc}. Since the forward bias diffusion current increases with higher recombination rates, more recombination translates to lower V_{oc}. The reverse saturation current is responsible for giving the recombination in forward bias. The quantity, velocity, and lifetime of the carriers determine the recombination rate.

The open-circuit voltage is dependent on the number of minority carriers at the junction edge. We need to minimize the equilibrium carrier concentration to decrease the recombination. This can be achieved by increasing the doping concentration of the wafer, thus increasing the V_{oc}. However, the open circuit voltage is also dependent on the diffusion length. If the diffusion length is too low, then many minority carriers will vanish quickly from the junction edge by recombination. This allows more carriers to cross and increases the forward bias current. A high diffusion length is needed in order to minimize the recombination and increase V_{oc}. The reality is that wafers with higher doping have shorter diffusion lengths. The tradeoff between diffusion length and doping concentration in obtaining a high V_{oc} is demonstrated in Figure 2.31.

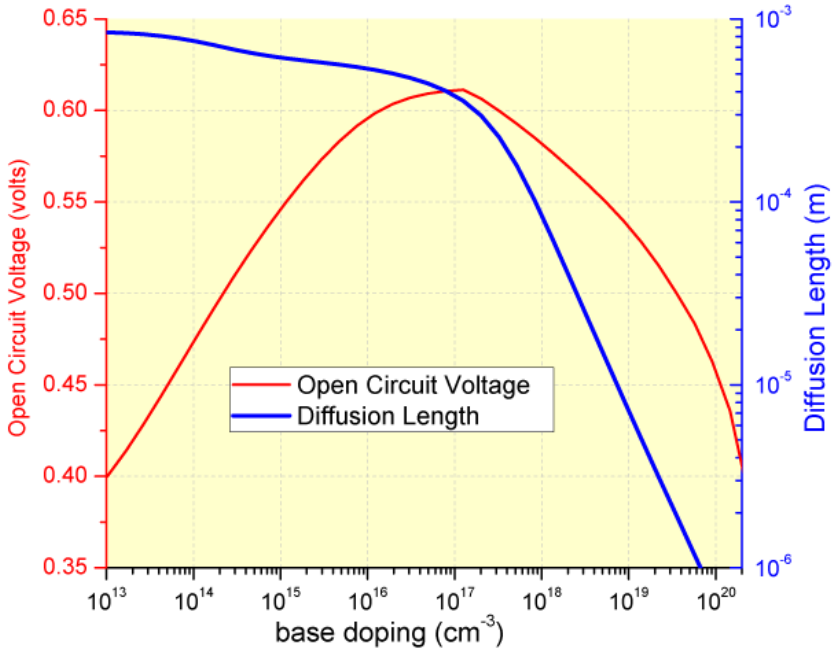

Figure 2.31 Tradeoff between diffusion length and doping concentration in achieving high open-circuit voltage [47]

The differences in diffusion length are plotted in Figure 2.32. The plot demonstrates that the diffusion length is considerably shorter at higher doping concentrations, as expected from theory.

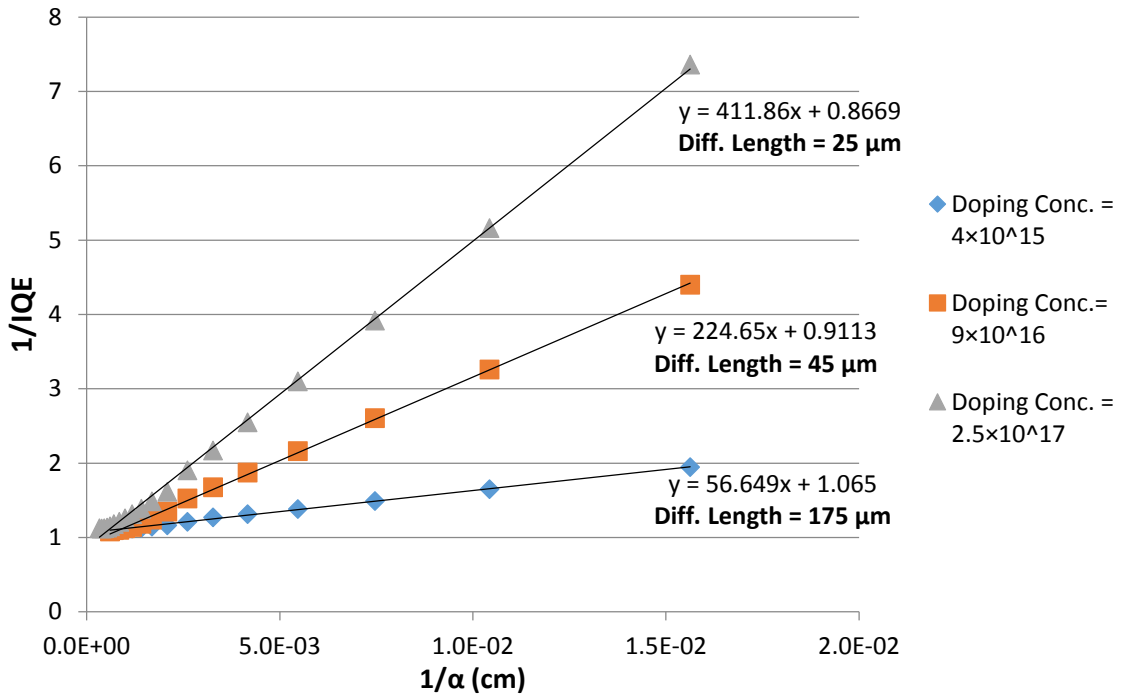

Figure 2.32 Comparison of diffusion lengths for wafers with different doping concentrations

The results from the HIT solar cells made on the different p-type wafers are summarized below in Table 2.1:

Table 2.1 Summary of the measurement results from the HIT solar cells made on wafers with different doping concentrations

Wafer Lot #, Specifications	978, University Wafer 1-10 Ω-cm Thickness: 380 µm	1412-3485, IWS 0.1-0.5 Ω-cm Thickness: 380 µm	2612, El-Cat 0.095-0.13 Ω-cm Thickness: 350 µm
Measured Resistivity (Ω-cm)	4.0	0.2	0.1
Calculated Doping Concentration (cm^{-3})	4×10^{15}	9×10^{16}	2.5×10^{17}
Open-Circuit Voltage (V)	0.58	0.63	0.59
Diffusion Length (µm)	175	45	25
Lifetime (µs)	13	1.1	0.4
Calculated V_{oc} (V)	0.58	0.63	0.62

The results obtained show that while increasing the doping concentration of the wafers used in n+/p/p+ HIT cells increases the open-circuit voltage to a point, the diffusion length is

decreasing at the same time, and the attainable open-circuit voltage is somewhat limited by this tradeoff. The measured V_{oc} of the first two wafers matched the theoretical calculations exactly. While the V_{oc} of the highest doped wafer did not match exactly with the calculation of expected V_{oc}, it is adequate to demonstrate the principle of V_{oc} being limited as the doping concentration becomes very high. The n+/p/p+ HIT solar cells made using wafers with moderate doping concentrations should have the best performance. Those made using very lightly-doped or heavily-doped wafers will likely encounter limitations.

CHAPTER 3: NANOCRYSTALLINE SILICON GERMANIUM DEVICES

3.1 Introduction to Nanocrystalline Silicon Germanium (nc-SiGe:H) Devices

Many research groups have successfully implemented multiple-junction solar cells with efficiencies near 15% using a-Si:H and nc-Si:H [48-51]. The a-Si:H portion of a tandem cell serves to absorb the short-wavelength light, and the nc-Si:H part is meant to absorb the longer-wavelength infrared and red light that has already passed through the a-Si:H section. One way to improve the infrared absorption is to increase the thickness of the nc-Si:H layer, but this also worsens the carrier collection. A stronger absorber in the infrared region is needed to improve efficiencies.

Hydrogenated nanocrystalline silicon germanium, or nc-SiGe:H, is a material with good absorption in the infrared region, even using thin layers. The bandgap of nc-SiGe:H is tunable from that of Si (~1.1 eV) to Ge (~0.7 eV) by changing the Ge content. Figure 3.1 shows the absorption spectra of nc-$Si_{(1-x)}Ge_x$ as the proportion of Ge to Si changes. The plot shows that nc-SiGe:H has a considerable advantage in absorption for the range where most solar irradiation occurs. This means that nc-SiGe:H could theoretically attain higher current densities than basic nc-Si:H in the infrared region. This material is also desirable for thin film transistors due to its tunable bandgap [52].

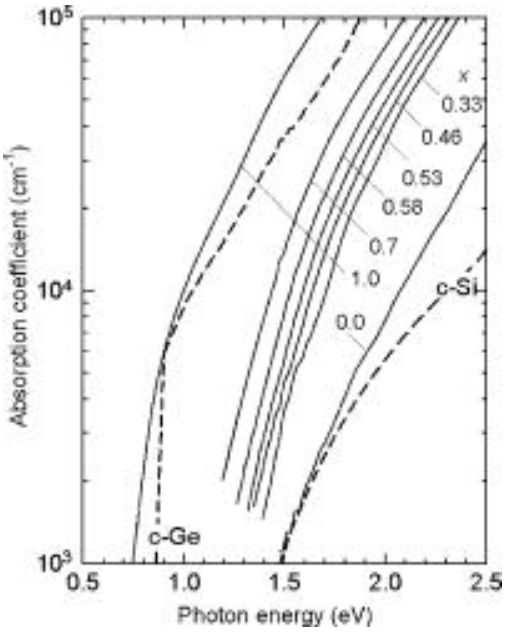

Figure 3.1 Absorption spectra of nc-Si$_{(1-x)}$Ge$_x$ films for different concentrations of Ge [53]

3.2 Literature Review

This section briefly explores the literature related to the deposition and characteristics of nc-SiGe:H.

3.2.1 Material Growth

A study on the growth of nc-SiGe:H was carried out by Ganguly et al. [54] while varying the PECVD parameters such as the power, hydrogen dilution, temperature, and pressure. They found that there is an optimum hydrogen dilution to achieve the largest grain size for each temperature, shown in Figure 3.2. The optimization of the hydrogen dilution would imply that the hydrogen is not only involved in the formation of crystallites, but also in ion bombardment which disrupts the crystal growth. When these two processes are balanced, then the largest possible crystallites can be formed at each temperature. Also, the observation that the optimum hydrogen dilution decreases with temperature suggests that the hydrogen is aiding in giving the energy needed to form crystals at low temperatures. Figure 3.3 shows their

study of grain size vs. hydrogen dilution at different pressures. They observed that the nc-SiGe:H exhibited a larger grain size than nc-Si:H at higher hydrogen dilution. This was explained by Dalal in nc-Ge:H films [55]. Since the Ge-H bond is weaker than the Si-H bond, the H_2 desorbs more easily from the Ge-H bond and the grain size is larger in nc-Ge:H films.

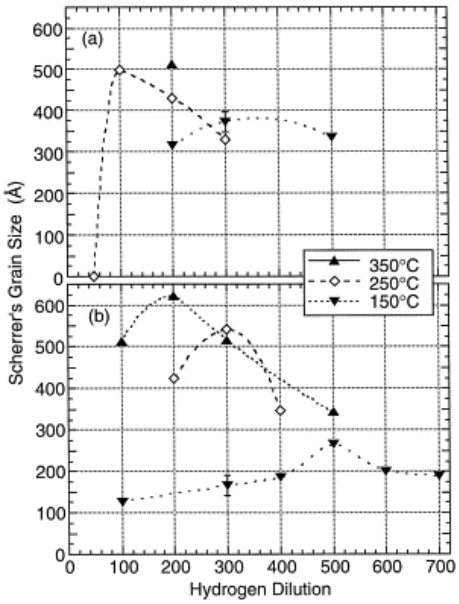

Figure 3.2 Grain sizes vs. hydrogen dilution for nc-SiGe:H samples deposited at (a) 0.5mT, 89mW/cm^2 and (b) 0.9mT, 637mW/cm^2 at different temperatures [54]

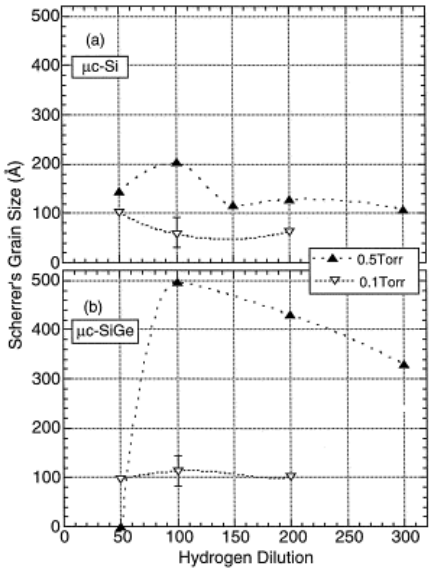

Figure 3.3 Grain sizes versus hydrogen dilution for (a) nc-Si:H and (b) nc-SiGe:H deposited at 250°C [54]

Houben et al. reported on the Raman spectra of nc-SiGe:H PECVD films for varying Ge content [56], shown in Figure 3.4. They concluded that high content of Ge results in good crystallinity of the Ge-Ge crystals. In addition, they reported that nc-SiGe:H films exhibit conical crystals embedded in an amorphous matrix in early growth stages, and a fine-grain structure made up of faulted single-crystal columns.

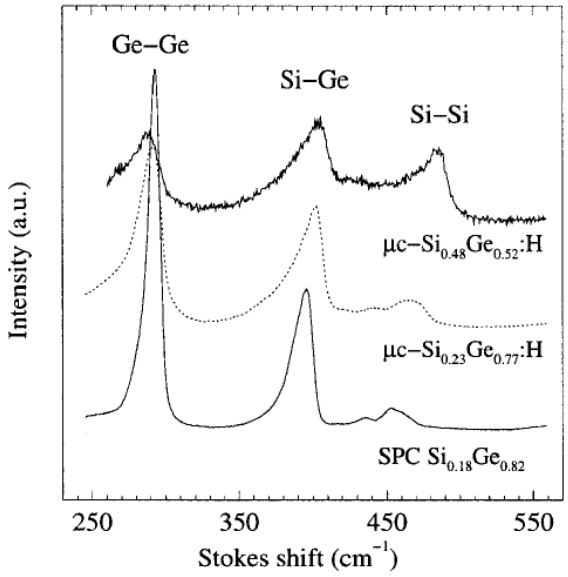

Figure 3.4 Raman spectra of nc-SiGe:H films with varying Ge content [56]

3.3 Fabrication Process

This section explains the process for fabrication of the nc-SiGe:H solar cells. Some aspects of the process that are similar to the HIT process are referred to from the previous chapter.

3.3.1 Plasma Enhanced Chemical Vapor Deposition (PECVD)

The PECVD process has already been discussed in Section 2.3.1.

3.3.2 Sample Preparation

Nanocrystalline Si and SiGe devices are generally deposited on electropolished stainless steel substrates. The pre-cleaning for these substrates is the same as for the HIT

samples discussed in Section 2.3.2. The loading, purging, and dummy plasma layer procedure are also the same as for HIT samples.

The first layer deposited is an a-Si n+ layer (0.3 µm thick) using 0.5% phosphine (PH_3). This layer functions as the back contact. Next, a thin layer of a-Si lightly doped with PH_3 is deposited to act as the seed layer for the nc-Si, which is gradually graded to nc-SiGe with the desired germanium content. The seed layer functions to provide nucleation sites and prevent phosphorous from diffusing into the main intrinsic layer [57]. A high hydrogen dilution is initially used to aid in formation of the nucleation centers and jumpstart the onset of crystallization. As the film grows, the hydrogen dilution ratio is gradually reduced to sustain the optimal crystallinity of the intrinsic layer. After the intrinsic layer, a thin layer of nc-SiGe:H p+ is grown, with a similar proportion of Ge as the i-layer to match the bandgap and make the transition smooth. The basic structure of a typical nc-SiGe:H device is shown in Figure 3.5.

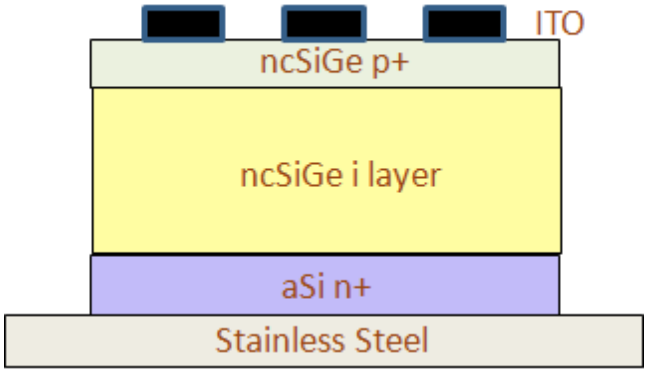

Figure 3.5 Device structure of nc-SiGe:H solar cell [58]

The i-layer is graded with ppm levels of phosphine and trimethylborane (TMB) to enhance the carrier range and to aid in hindering oxygen from going into the i-layer. To prevent post-deposition oxidation through the grain boundaries, a thin cap layer of a-SiGe is deposited on the i-layer. This also improves the open-circuit voltage by decreasing the reverse saturation

current. The p+ layer is composed of an amorphous seed layer, followed by a nanocrystalline layer, finished with an amorphous cap layer. The p+ is heavily doped with boron using diborane to make a good ohmic contact. During the deposition of the p+ layer, relatively lower temperature is used to ensure that the boron does not diffuse into the i-layer. The top contact, as with HIT, consists of indium tin oxide (ITO) which is deposited via sputtering. The energy band diagram of the cell is shown in Figure 3.6.

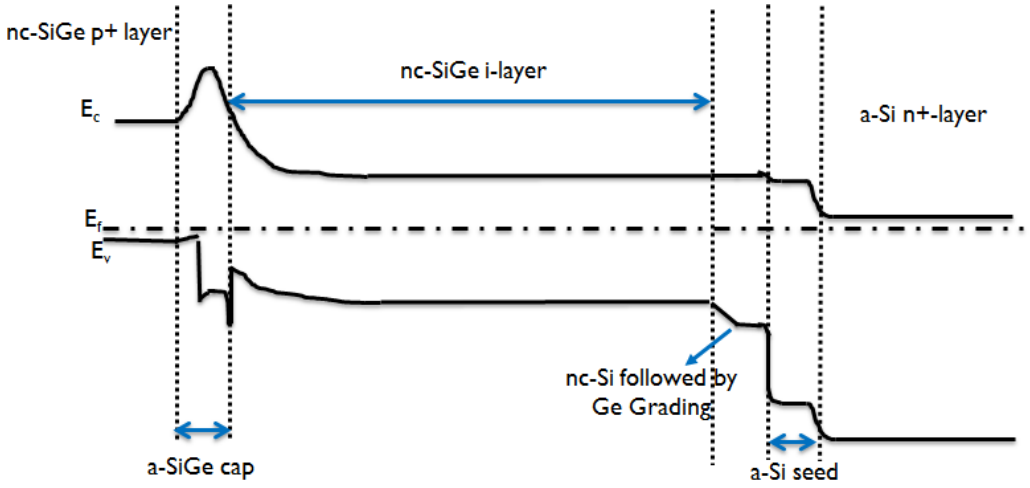

Figure 3.6 Energy band diagram of nc-SiGe:H solar cell [37]

3.3.3 Sputtering

The procedure for the sputtering of the ITO for a top contact to nanocrystalline devices is the same as for HIT, described in Section 2.3.3.

3.4 Measurement Techniques

The measurement techniques discussed in this section are the techniques performed only on nc-SiGe:H films and devices. Some measurements that are common to both HIT and nc-SiGe:H devices have already been discussed in Section 2.4.

3.4.1 Optical Spectroscopy

Optical spectroscopy can be performed on thin films to determine the thickness and understand their reflection, transmission, and absorption properties. The reflection spectrum of a thin film will have a series of interference peaks due to reflection from two different surfaces (front and back), and the distance between adjacent crests or troughs can be used to calculate the thickness of the film. Figure 3.7 shows the reflection data for a typical thin film sample. The thickness of the film can be calculated using the following formula [59].

$$t = \frac{\lambda_1 \times \lambda_2}{2(n_1 \times \lambda_2 - n_2 \times \lambda_1)}$$

where λ_1 and λ_2 are the wavelengths corresponding to two adjacent crests or troughs with refractive indices of n_1 and n_2, respectively.

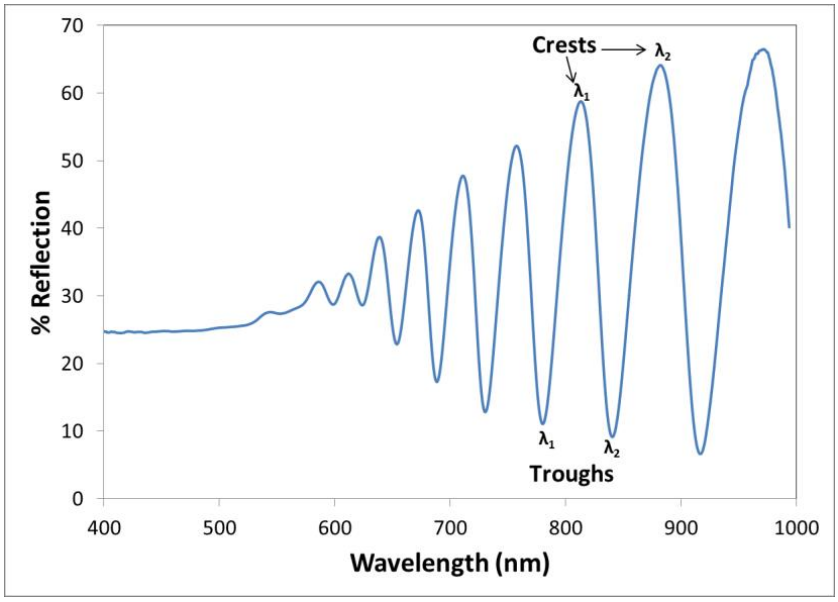

Figure 3.7 Reflection data for a typical thin film sample

3.4.2 Raman Spectroscopy

Raman spectroscopy is a useful tool for measurement of the crystallinity of a material. When light is incident upon a solid, there will be phonons that scatter elastically and phonons that scatter inelastically. The majority of the phonons will undergo elastic scattering, also

known as Raleigh scattering. However, we are concerned with the inelastic scattering, which is responsible for causing lattice vibrations and the production of phonons that cause an energy shift for the incident photons. This phenomenon, as described by Iqbal and Veprek [60], is known as Raman shift. Figure 3.8 visualizes the different scattering types.

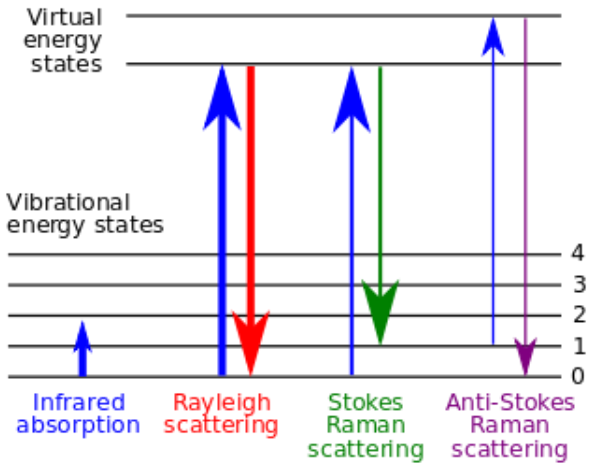

Figure 3.8 Scattering phenomena of incident light in a material [37]

In crystalline silicon, the only optical phonons with zero momentum are the ones with 64 meV energy, resulting in a sharp peak at 520 cm^{-1}. However, in amorphous silicon, there is a band of energies over which momentum is conserved; the band of small peaks combines to make a broader spectrum with a peak around 480 cm^{-1}. Figure 3.9 shows a comparison of the Raman spectra for different phases of silicon.

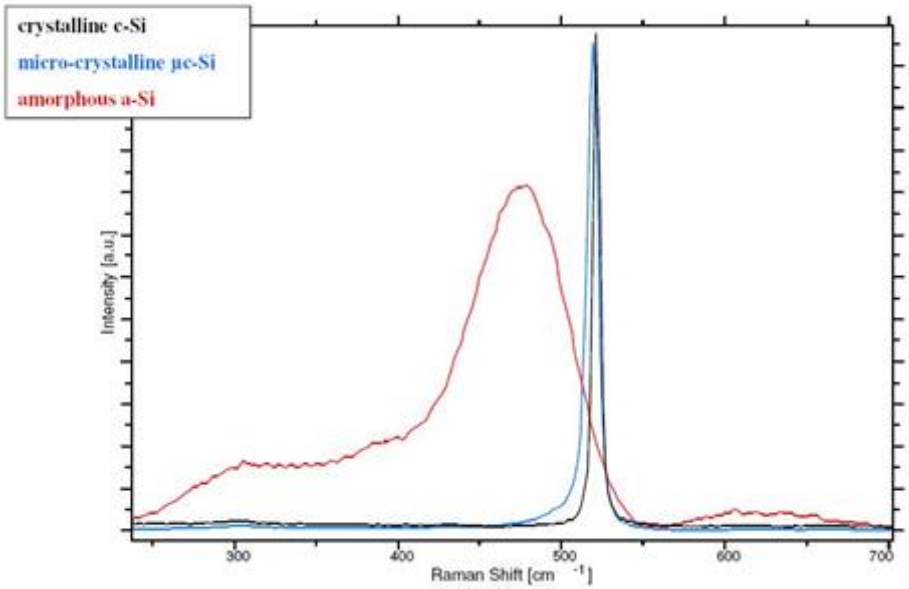

Figure 3.9 Raman spectra for the different phases of silicon

When fitting curves to the peaks, we see that the amorphous silicon peak is a broad Gaussian-type peak, due to disorder in the bond lengths. On the other hand, the crystalline peak is a good fit for a Lorentzian peak because there is not much variation in the bond length. The peak analysis consists of separating the amorphous and crystalline peaks from the total intensity curve and comparing the obtained heights of the individual peaks [61]. The area is not comparable, due to the peaks being of different types, but the heights of the peaks are good indicators of the proportion of crystallinity in nanocrystalline silicon.

3.4.3 Capacitance-Frequency (CF) Measurements

The measurement of capacitance versus frequency is a useful method of studying the defect density profile in thin film solar cells, as explained by Walter et al. [62]. Deeper traps in the bandgap emit over a longer time than shallower traps near the band edge. Using this principle, we can measure the trap density by differential capacitance techniques. Figure 3.10 shows a diagram of the emission phenomenon. Measurements at lower frequencies are able to

reach deep into the bandgap and detect both the fast-emitting and medium-emitting traps. Measurements at higher frequencies will only detect the fast-emitting traps, which are close to the band edges. If the curve of capacitance vs. frequency is differentiated with respect to frequency, then a profile of the traps can be built, according to the traps' respective location as compared with the band edge.

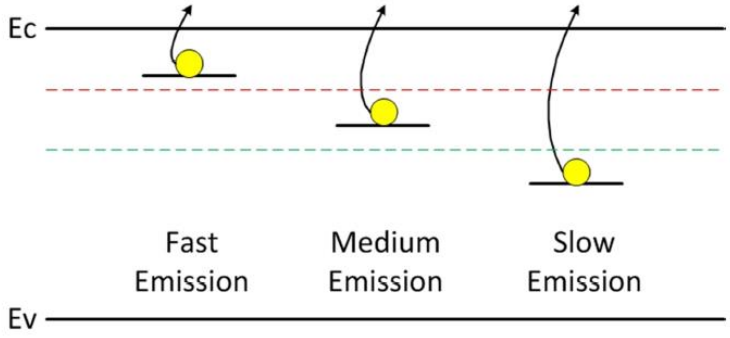

Figure 3.10 Diagram of emission within the bandgap [63]

Based on the basic carrier conservation, we can calculate the capacitance contribution from a single trap [62]. After integrating over energy and space, we can solve for the number of traps according to the equation:

$$N_t(E_\omega) = -\frac{V_{bi}}{qw}\frac{dC}{d\omega}\frac{\omega}{kT}$$

where E_ω is the demarcation energy, V_{bi} is the built-in voltage, q is the charge of an electron, C is the capacitance, w is the width of the i-layer, ω is the frequency, k is Boltzmann's constant, and T is the temperature. The demarcation energy E_ω is the energy at which traps can respond to a given frequency, as defined by the formula:

$$E_\omega = kT\ln(\frac{\omega_0}{\omega})$$

where ω_0 is the attempt-to-escape frequency of the material. This concept is discussed in more detail in Section 3.4.4.

Using the equations above, we can use CF measurements to obtain the defect density profile of a sample. Shown in Figure 3.11 is a CF measurement performed on a nc-Si:H solar cell at room temperature, along with the calculated resulting defect density profile. The peak density of defects occurs around 0.55 eV, which is the midgap energy level of nc-Si, having a bandgap of 1.1 eV [64].

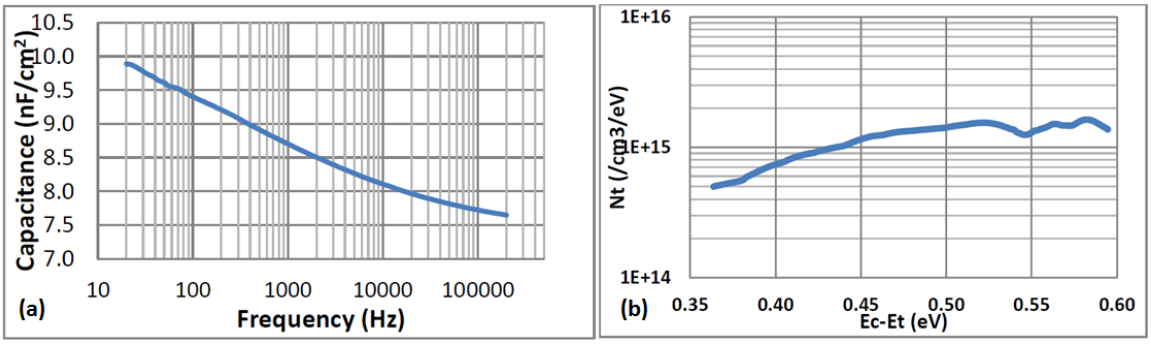

Figure 3.11 (a) Capacitance vs. Frequency and (b) Defect profile for nc-Si sample measured at room temperature [64]

3.4.4 Capacitance-Frequency vs. Temperature (CFT) Measurements

To determine the total amount of defects of a material, it is necessary to profile the traps from the band edge to past midgap. Capacitance-frequency measurements consequently need to be done at low frequency or high temperature to reach deeper into the bandgap. The equations for CFT have been described by Heath [65] At 20 Hz and 100°C in nc-Si, the responding traps correspond to 0.8 eV below the band edge [66]. Since the demarcation energy E_ω (introduced in Section 3.4.3) is dependent upon both temperature and frequency, we can use CFT measurements to more effectively model the defects throughout the bandgap.

The CFT measurements were done using an in-house built experimental setup, utilizing a Hioki LCR meter with an operating range of 1 mHz – 200 kHz, listed with 0.05% basic accuracy. The setup is pictured in Figure 3.12. Although the measurement range of the LCR

meter was rated at 1 mHz – 200 kHz, in practice the usable range was frequently limited by the sample itself. At very low frequencies leakage can cause high dissipation values [67], and at very high frequencies inductance effects are possible [68], so the data at the extremes of the frequency range were neglected. To adjust the sample temperature between 100 and 400 K, we used a continuous-flow liquid nitrogen cryostat, which was run by a Lakeshore 331 temperature controller. To accurately monitor the sample temperature, one platinum resistance temperature detector (RTD) was mounted on the surface of the sample and two more RTDs were contained within the head of the cryostat itself.

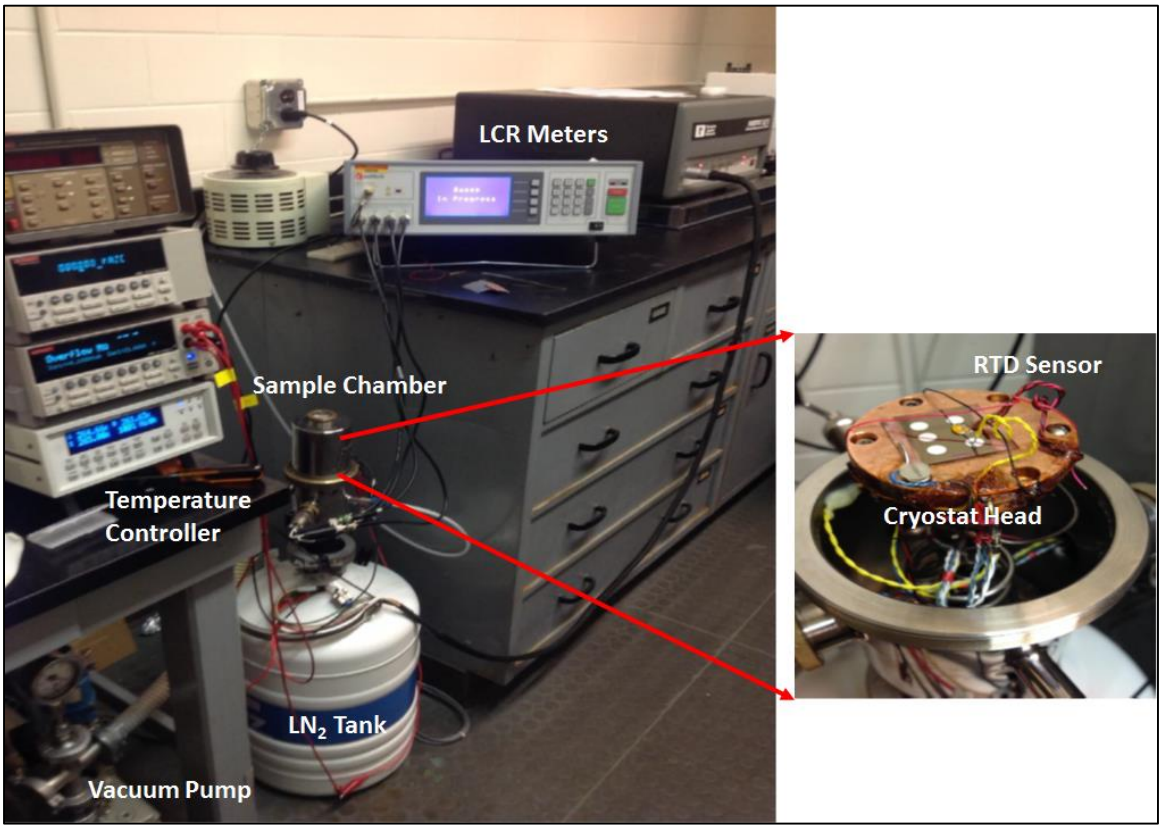

Figure 3.12 Experimental setup for CFT measurement. Inset: Details of the cryostat stage inside the sample chamber [69]

Figure 3.12 shows a sample that has been mounted for measurement, resting directly upon the cryostat head. To improve the thermal conductivity between the cryostat head and the

sample, we apply cryogenic rated grease, which solidifies at low temperatures. A wire probe is connected to the top of the sample, and the RTD connects in a similar manner to ensure that the temperature measurement is accurate. A silver wire is clamped to the top contact and thick copper wire is connected to the bottom contact. The wires from the probes are wrapped around the cryostat head and varnished to ensure that they cool to the set temperature.

Since the measurement of CFT involves deep energy levels and their responses, we must consider the carrier capture and emission rates. The emission rate of electrons trapped by defects in the bandgap, assuming we have a thermally activated process, can be determined by the equation:

$$e_n = N_c \nu_{th} \sigma_n \exp\left(-\frac{E_A}{kT}\right)$$

where N_c is the density of states in the conduction band, ν_{th} is the thermal velocity, σ_n is the capture cross-section, E_A is the trap activation energy, and k and T are Boltzmann's constant and temperature, respectively [65, 70]. The above equation is an Arrhenius equation, where the emission rate depends upon the pre-exponential factor ($N_c \nu_{th} \sigma_n$, also known as ν_0, which is the attempt-to-escape frequency, or ATE frequency), the measurement temperature, and the activation energy [65]. Accurate calculation of the ATE frequency is vital for precise modeling of the trap energy levels in the material. Plotting $\ln(e_n)$ versus $1/T$ on an Arrhenius plot yields a straight line whose slope corresponds to the trap activation energy (E_A) and whose intercept corresponds to the capture cross-section (σ_n) and subsequently the ATE frequency (ν_0). However, the use of this technique assumes that the pre-exponential factor is not dependent on temperature. In reality, $N_c \propto T^{3/2}$ and $\nu_{th} \propto T^{1/2}$, meaning that the ATE frequency inherently depends on temperature. This being the situation, we write the pre-exponential factor as ΥT^2, where:

$$\gamma = N_c v_{th} \sigma_n T^{-2}$$

Consequently, the emission rate becomes:

$$e_n = \gamma T^2 \exp\left(-\frac{E_A}{kT}\right)$$

The temperature dependence in the exponential term ends up dominating the squared temperature term in the pre-factor, and γT^2 value is often quite similar to the value of the ATE (ν_0) frequency. This being the case, the temperature dependence from the squared term is often neglected. However, we estimate the defect density using both methods.

Using capacitance measurements, we can study the change in trap emission with changes in the measurement temperature. As the frequency is varied from high to low, the capacitance increases due to more states responding. CFT curves of a sample are shown in Figure 3.13. Part (a) summarizes the capacitance curves for a variety of temperatures, and each curve in part (b) is the differential capacitance (*–fdC/df*) having peaks where the slope changes the most rapidly in part (a).

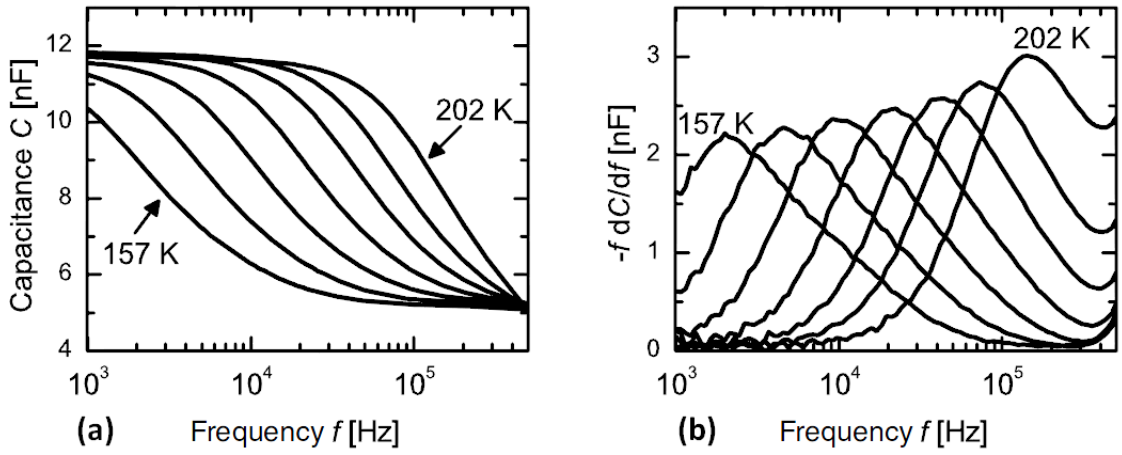

Figure 3.13 (a) Capacitance vs. Frequency, (b) Differential Capacitance vs. Frequency for various temperatures in a thin film solar cell [65]

When we plot the frequencies at which the differential peaks occur as a function of *1/T*, we see that the curve is Arrhenius in nature, as shown in Figure 3.14. As mentioned before, the slope of this line corresponds to the activation energy, and the intercept of the line corresponds to the capture cross-section (σ_n), from which the ATE frequency (ν_0) can be computed. Making use of the (*–fdC/df*) differential values and the calculated ATE value, we can model the defect density profile throughout the bandgap.

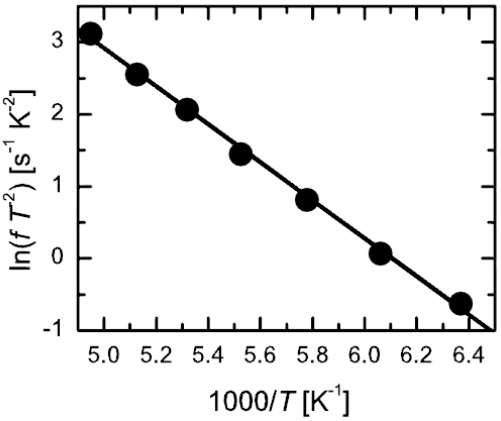

Figure 3.14 Arrhenius plot of the capacitance peak frequencies for the different measurement temperatures [65]

3.4.5 Other Measurements

The other measurements performed on nc-SiGe:H devices, such as IV, QE, and CV, have already been discussed in Section 2.4.

3.5 Results

This section discusses the results of measuring the defect density spectrum on a nc-SiGe:H device made with 35% Ge. The performance of thin film solar cells depends strongly upon the material defects present. The carrier lifetime and QE are reduced by defects, due to the trap energy levels created deep in the bandgap. It is important to know the defect properties in order to understand the device physics of the solar cell.

The CF measurement of the cell with germanium content $X_{Ge} = 0.35$ is shown in Figure 3.15, along with two other cells having different germanium content for comparison. The plot demonstrates that the defect density increases with the germanium content. This behavior can be explained by the fact that the mismatch in bond length in the atomic structure causes more defects with more germanium present.

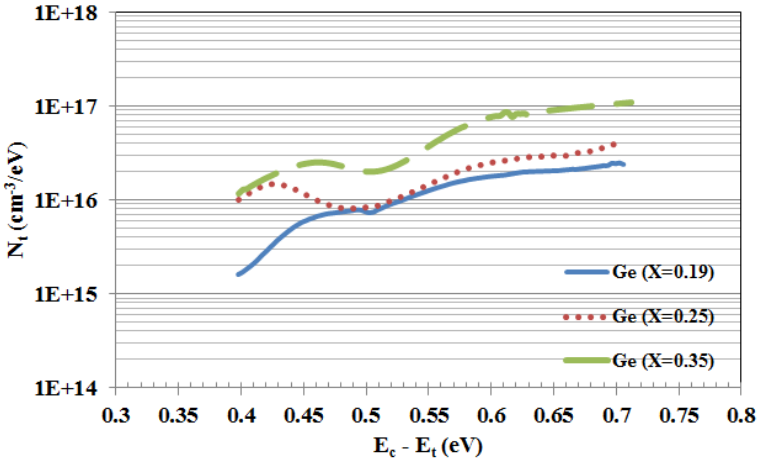

Figure 3.15 Defect density vs. energy below conduction band for different Ge content

Using CF for a variety of temperatures (CFT), we can see a broader view of the defect density spectrum. It is important to know the distribution of the defects across the bandgap and the ways to counteract the defects. Investigating the defects with CFT measurement helps us to effectively evaluate the defects present in the solar cell. Figure 3.16 shows the measured data from CFT for the nc-SiGe:H solar cell with germanium content $X_{Ge} = 0.35$. The CF spectrum shifts toward the left as the temperature falls below 300 K. The capacitance increase at higher temperatures implies that the presence of Ge causes deep defects, as was shown in Figure 3.15 above. We observe two sets of peaks (denoted with arrows) in the differential capacitance curves corresponding to the two bands in the CFT data. The lower set of peaks relate to the geometric capacitance step after the initial free carrier response having activation

energy equal to the Fermi level. The higher set of peaks relates to the deep traps resulting from the presence of Ge.

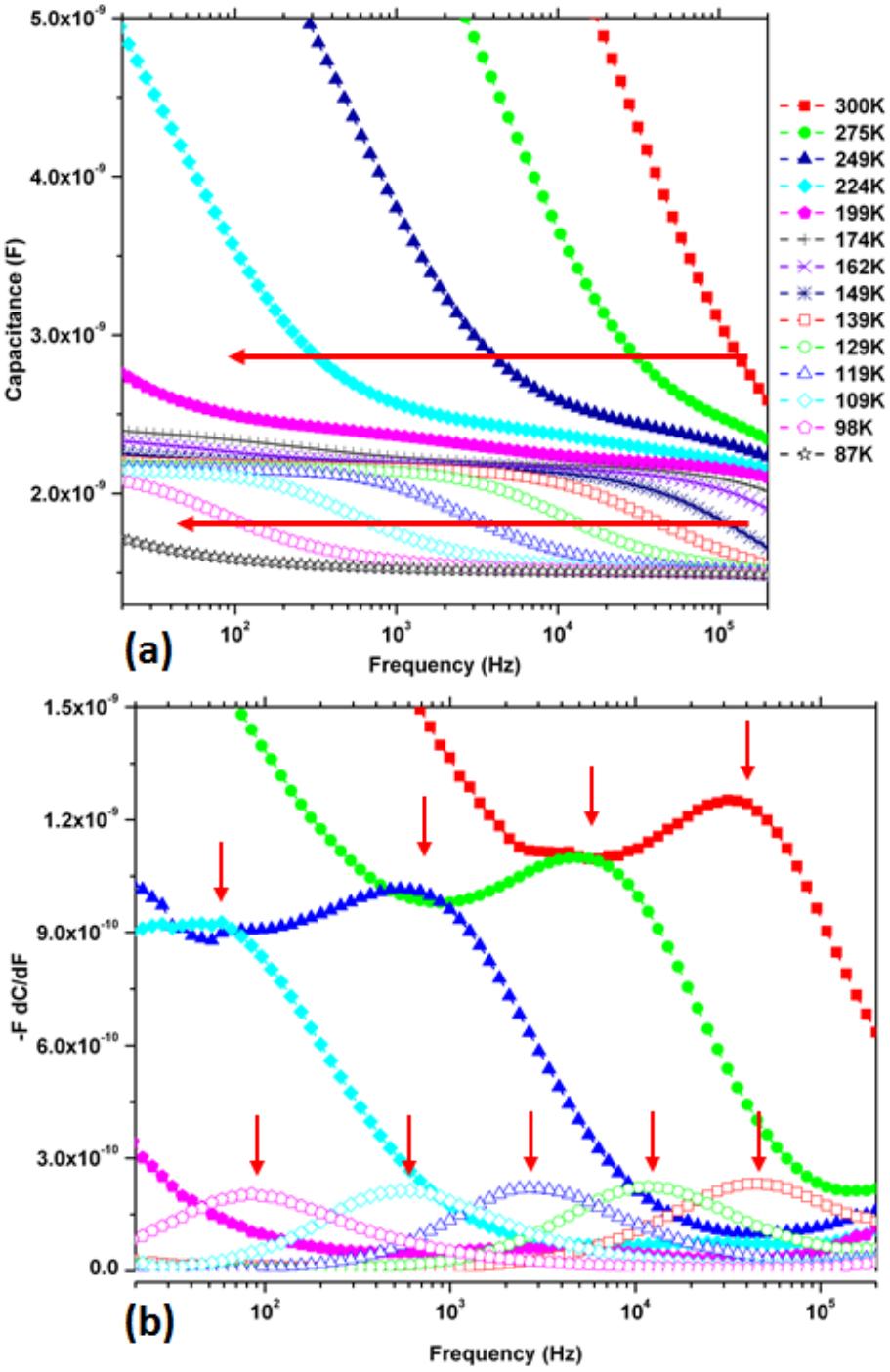

Figure 3.16 (a) CFT data for the nc-SiGe:H solar cell, X_{Ge}=0.35. The arrows indicate the capacitance shift due to the two different trap levels. (b) Differential capacitance curves vs. frequency. The arrows signify emission peaks.

The frequencies where the peaks occur are plotted as a function of the inverse of temperature in Figure 3.17. We can calculate the activation energies of both sets of peaks and the ATE frequency from the slope of the Arrhenius plot. The pre-exponential factor with a T^2 dependence is calculated from the intercept.

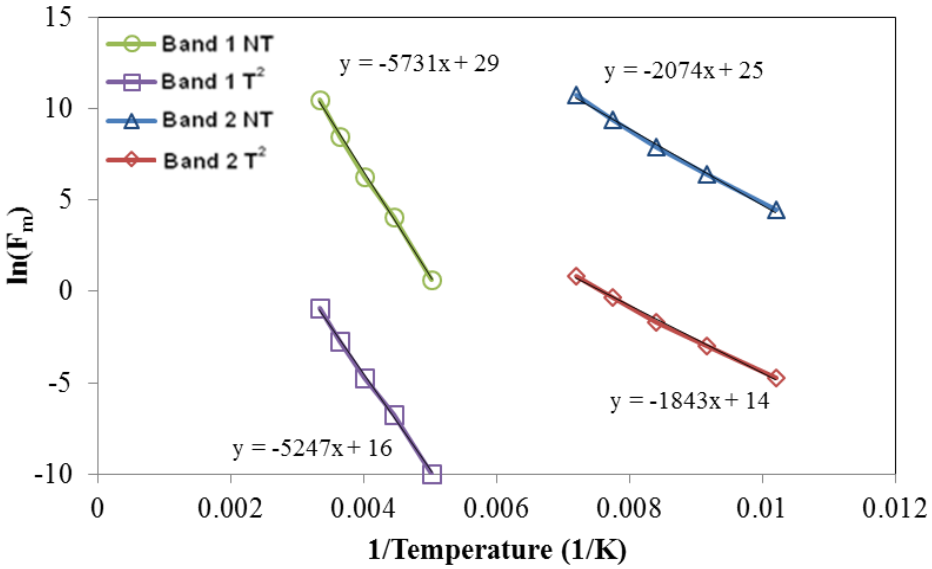

Figure 3.17 Arrhenius plot of the differential capacitance peak frequencies as a function of 1/T for the nc-SiGe:H solar cell (X_{Ge}=0.35)

It is observed that the carrier response band centers around 190 meV, and the ATE value is about 5×10^{11} Hz. The second band (corresponding to the deep defects) centered around 450 meV, and its ATE value was approximately 3×10^{12} Hz. These results are tabulated below in Table 3.1.

Table 3.1 Summary of parameters calculated from CFT data of nc-SiGe:H cell (X_{Ge}=0.35)

	Carrier Response	**Deep Defect Response**
Activation Energy, E_a	190 meV	452 meV
ATE, ν_0	5×10^{11} Hz	3×10^{12} Hz
Pre-factor, Υ	3.7×10^{7} Hz K^{-2}	1.4×10^{7} Hz K^{-2}
Capture cross-section, σ_n^*	5.1×10^{-15} cm^2	3×10^{-14} cm^2

Using the calculated ATE frequency, the defect density spectrum of the nc-SiGe:H solar cell can be estimated, shown in Figure 3.18. The carrier response peak at 190 meV has a

defect density of about 1×10^{16} cm^{-3} eV^{-1}. The red line indicates the Fermi energy level. There is a small peak around 350 meV, also observed in nc-Si:H. However, this peak is dwarfed by a larger peak around 450 meV that has a defect density of about 2×10^{16} cm^{-3} eV^{-1}. This larger peak is possibly due to the presence of Ge. It is observed that the midgap defects for nc-SiGe:H are considerable, much higher than in regular nc-Si:H. For comparison, the defect density spectrum of nc-Si:H without Ge is shown in Figure 3.19.

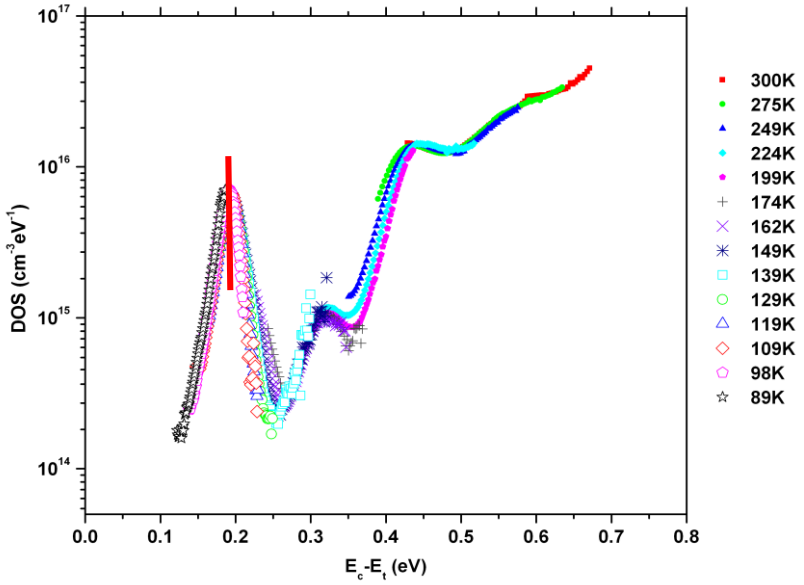

Figure 3.18 Calculated defect density profile of the nc-SiGe:H solar cell (X_{Ge}=0.35)

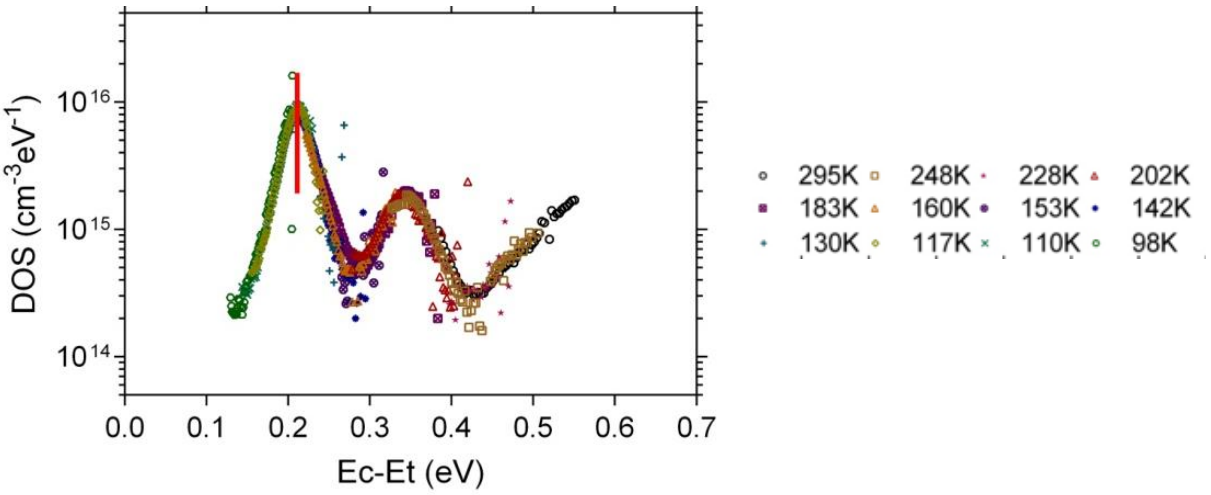

Figure 3.19 Calculated defect density profile of nc-Si:H solar cell (no Ge)

CHAPTER 4: SUMMARY

The primary objective of this work was to study the fundamental properties of n+/p/p+ HIT solar cells and to investigate the defect density spectrum in nc-SiGe:H solar cells.

- In n+/p/p+ HIT solar cells, we have demonstrated the relationship between the doping concentration of the wafer and the attained open-circuit voltage. The open-circuit voltage increases with doping concentration until the recombination losses negatively affect the voltage.
- We have also verified the relationship between the doping concentration of the wafer and the minority carrier diffusion length and lifetime in n+/p/p+ HIT solar cells. It is observed that the diffusion length and lifetime drop substantially as the doping concentration increases.
- The defect density spectrum of nc-SiGe:H solar cells is estimated using measured CFT data and the calculated ATE frequency. This led to an understanding of the midgap and tail states in nc-SiGe:H. It is inferred that the Ge present is responsible for high defect densities in the midgap.

REFERENCES

[1] http://www.ren21.net/Status-of-Renewables/Global-Status-Report/, accessed on 06/30/15 (2015)

[2] R.C. Chittick, J.H. Alexander and H.F. Sterling, "Preparation and properties of amorphous silicon", Journal of the Electrochemical Society, 116 (1), 77-81 (1969)

[3] B. Abeles, G.D. Cody, Y. Goldstein, T. Tiedje, C.R. Wronski, "Hydrogenated amorphous silicon solar cells", Thin Solid Films, 90 (4), 441-449 (1982)

[4] H. Keppner, J. Meier, P. Torres, D. Fischer and A. Shah, "Microcrystalline silicon and micromorph tandem solar cells", Applied Physics A, 69 (2), 169-177 (1999)

[5] http://greentechresearch.wordpress.com/2013/06/07/solar-cells-a-shining-technology-between-politics-and-science/, accessed 06/30/15 (2013)

[6] A. Shah, J. Meier, E, Vallat-Sauvain, N. Wyrsch, U. Kroll, C. Droz and U. Graf, "Material and Solar cell research in microcrystalline silicon", Solar Energy Materials and Solar Cells, 78, 469-491 (2003)

[7] S. Klein, F. Finger, R. Carius, T. Dylla, B. Rech, M. Grimm, L. Houben and M. Stutzmann, "Intrinsic microcrystalline silicon prepared by hot-wire chemical vapour deposition for thin film solar cells", Thin Solid Films, 430 (1–2), 202-207 (2003)

[8] Panasonic Press Release, 10 April 2014. "Panasonic HIT® solar cell achieves world's highest energy conversion efficiency of 25.6% at research level" (http:// panasonic.co.jp/corp/news/official.data/data.dir/2014/04/) (2014)

[9] J. Zhao, A. Wang, M.A. Green, F. Ferrazza. "Novel 19.8% efficient 'honeycomb' textured multicrystalline and 24.4% monocrystalline silicon solar cells", Applied Physics Letters 73: 1991–1993 (1998)

[10] http://panasonic.net/ecosolutions/solar/hit/, accessed on 06/30/15 (2015)

[11] A. Datta, M. Rahmouni, M. Nath et al., "Insights gained from computer modeling of heterojunction with instrinsic thin layer 'HIT' solar cells", Solar Energy Materials & Solar Cells 94 (9) 1457–1462 (2010)

[12] M. Kushner. Journal of Applied Physics 63:2532 (1988)

[13] A. Gallagher. Journal of Applied Physics 63:2406 (1988)

[14] M. C. M. van de Sanden, W.M.M. Kessels, A.H. Smets, R.J. Severens, D.C. Schramm, Proceedings of Materials Research Society 557:13 (1999)

[15] M. Pontoh, V. L. Dalal, N. Gandhi. Proceedings of Materials Research Society 715:A19.6 (2002)

[16] E. A. G. Hamers, W. G. van Sark, J. Bezemer, H. Meiling, W. F. van der Weg. Journal of Non-Crystalline Solids 226:205 (1998)

[17] J. R. Doyle, D. Doughty, A. Gallagher. Journal of Applied Physics 68:4375 (1990)

[18] A. Matsuda, K. Tanaka. Journal of Non-Crystalline Solids 97–98:1367 (1987)

[19] J. Perrin, G. Brunno, P. Capezzuto, A. Madan, "Plasma deposition of a-Si materials", San Diego: Academic, p. 216 (1995)

[20] J. Robertson, Journal of Non-Crystalline Solids 266–269:79 (2000)

[21] A. Matsuda, Journal of Non-Crystalline Solids 59-60 767 (1983)

[22] J. Perrin, M. Shiratani, P. Kae-Nune, H. Videlot, J. Jolly, J. Guillon, J. Vac. Journal of Science and Technology A16 278 (1998)

[23] V. Dalal, "Fundamental considerations regarding the growth of amorphous and microcrystalline silicon and alloy films", Thin Solid Films 395 173–177 (2001)

[24] V. Dalal, S. Kaushal, T. Maxson, R. Girvan, A. Boerner. Proceedings of the American Institute of Physics 394 33 (1997)

[25] W. M. M. Kessels, A.H.M. Smets, B.A. Korevaar, G.A. Adriaenssens, M.C.M. Van den Sanden, D.C. Schram. Materials Research Society Proceedings 557 35 (1999)

[26] S. Lien, Y. Chang, Y. Cho, Y. Chang, and S. Lee, "Deposition and characterization of high-efficiency silicon thin-film solar cells by HF-PECVD and OES technology", IEEE Transactions on Electronic Devices 5 59 (2012)

[27] V. Dalal, "Growth chemistry of amorphous silicon and amorphous silicon–germanium alloys", Current Opinion in Solid State and Materials Science 6 455–464 (2002)

[28] W. M. M. Kessels, M.C.M. van de Sanden, R.J. Severens, L.J. van Ijzendoorn, D.C. Schramm. Proceedings of Materials Research Society 507-529 (1998)

[29] M. Tanaka et al. Journal of Applied Physics 31 3518 (1992)

[30] Y. Tsunomura, Y. Yoshimine, M. Taguchi, T. Baba, T. Kinoshita, H. Kanno, H. Sakata, E. Maruyama, M. Tanaka, "Twenty-two percent efficiency HIT solar cell", Solar Energy Materials & Solar Cells 93 670–673 (2009)

[31] K. Wakisaka, M. Taguchi, T. Sawada, M. Tanaka, T. Matsuyama, T. Matsuoka, S. Tsuda, S. Nakano, Y. Kishi and Y. Kuwano, "More than 16% solar cells with a new 'HIT' (doped a-Si / non-doped a-Si / crystalline Si) structure", Conference Record, the 22nd IEEE PVSC, 887-892 (1991)

[32] T. Mishima, M. Taguchi, H. Sakata, E. Maruyama, “Development status of high-efficiency HIT solar cells”, Solar Energy Materials & Solar Cells 95 18–21 (2011)

[33] H. Inoue, Y. Tsunomura, D. Fujishima, A. Yano, S. Taira, Y. Ishikawa, T. Nishiwaki, T. Nakashima, T. Asaumi, M. Taguchi, H. Sakata, E. Maruyama, “Improving the conversion efficiency and decreasing the thickness of the HIT solar cell”, Proceedings of Materials Research Society, in press (2009)

[34] J. Robertson, “Growth mechanism of hydrogenated amorphous silicon”, Journal of Non-Crystalline Solids, 266, 79-83 (2000)

[35] J. Dutta, U. Kroll, P. Chabloz, A. Shah, A. A. Howling, J. L. Dorier and Ch. Hollenstein, “Dependence of intrinsic stress in hydrogenated amorphous silicon on excitation frequency in a plasma-enhanced chemical vapor deposition process”, Journal of Applied Physics, 72, 3220-3222 (1992)

[36] E. Amanatides, D. Mataras and D. E. Rapakoulias, “Effect of frequency in the deposition of microcrystalline silicon from silane discharges”, Journal of Applied Physics, 90, 5799-5807 (2001)

[37] S. Konduri, “Study of transport properties and defect density profile in nanocrystalline silicon germanium devices”, PhD Thesis, Iowa State University (2014)

[38] http://www.jeol.co.jp/en/science/eb.html, accessed on 06/30/15 (2015)

[39] http://www.pveducation.org/pvcdrom/solar-cell-operation/fill-factor, accessed on 06/30/15 (2015)

[40] J. Bailat, E. Vallat-Sauvain, L. Feitknecht, C. Droz, and A. Shah , “Microstructure and open-circuit voltage of n−i−p microcrystalline silicon solar cells”, Journal of Applied Physics, 93, 5727 (2003)

[41] https://pvpmc.sandia.gov/modeling-steps/2-dc-module-iv/diode-equivalent-circuit-models/, accessed on 06/30/15 (2014)

[42] http://pveducation.org/pvcdrom/solar-cell-operation/quantum-efficiency, accessed on 06/30/15 (2015)

[43] V. Dalal, M. Leonard, J. Booker and A. Vaseashta, “Quantum efficiency of aSi:H alloy solar cells”, IEEE, 837 (1985)

[44] L. C. Kimerling, “Influence of deep traps on the measurement of free-carrier distributions in semiconductors by junction capacitance techniques”, Journal of Applied Physics, 45, 1839 (1974)

[45] R. H. Kingston, “Switching time in junction diodes and junction transistors”, Proceedings of the IRE, 42(5), 829-834 (1954)

[46] B. G. Streetman and S. Banerjee, Solid State Electronic Devices, 6th Edition, 208-211, Prentice Hall, Englewood Cliffs, NJ (2005)

[47] http://www.pveducation.org/pvcdrom/design/voltage-losses-due-to-recombination, accessed on 06/30/15 (2015)

[48] A. Shah, J. Meier, E. Vallat-Sauvain, C. Droz, U. Kroll, N. Wyrsch, J. Guillet and U. Graf, "Microcrystalline silicon and 'micromorph' tandem solar cells", Thin Solid Films, 403–404, 179-187 (2002)

[49] J. Meier, S. Dubail, S. Golay, U. Kroll, S. Faÿ, E. Vallat-Sauvain, L. Feitknecht, J. Dubail and A. Shah, "Microcrystalline silicon and the impact on micromorph tandem solar cells", Solar Energy Materials and Solar Cells, 74 (1–4), 457-467 (2002)

[50] K. Yamamoto, A. Nakajima, M. Yoshimi, T. Sawada, S. Fukuda, T. Suezaki, M. Ichikawa, Y. Koi, M. Goto, T. Meguro, T. Matsuda, M. Kondo, T. Sasaki and Y. Tawada, "A high efficiency thin film silicon solar cell and module", Solar Energy, 77 (6), 939-949 (2004)

[51] G. Yue, B. Yan, L. Sivec, T. Su, Y. Zhou, J. Yang and S. Guha, "Hydrogenated Nanocrystalline Silicon based Solar Cell with 13.6% Stable Efficiency", Materials Research Society Proceedings, 1426, 33-38 (2012)

[52] J.A. Tsai, A. J. Tang, T. Noguchi and R. Reif, "Effects of Ge on Material and Electrical Properties of Polycrystalline $Si_{1-x}Ge_x$ for Thin-Film Transistors", Journal of the Electrochemical Society, 142, 3220 (1995)

[53] T. Matsui, M. Kondo, K. Ogata, T. Ozawa and M. Isomura, "Influence of alloy composition on carrier transport and solar cell properties of hydrogenated microcrystalline silicon-germanium thin films", Applied Physics Letters, 89, 142115 (2006)

[54] G. Ganguly, M. Fukawa, T. Ikeda and A. Matsuda, "A study of the growth-mechanism and properties of microcrystalline silicon–germanium", Journal of Non-Crystalline Solids, 227–230 (2), 1069-1073 (1998)

[55] X. Niu and V. Dalal, "Growth and properties of nanocrystalline germanium films", Journal of Applied Physics, 98, 096103 (2005)

[56] L. Houben, R. Carius , D. Lundszien, J. Folsch , F. Finger, M. Luysberg and H. Wagner, "Structural properties of microcrystalline silicon-germanium films", Philosophical Magazine Letters, 79 (2), 71-78 (1999)

[57] V. Dalal, K. Muthukrishnan, S. Saripalli, D. Stieler and M. Noack, "Growth and Electronic Properties of Nanocrystalline Si", Materials Research Society Proceedings, 910, 0910-A13-01 (2006)

[58] S. Konduri, W. Mulder, and V. Dalal, “Defects and doping in nanocrystalline silicon-germanium devices”, Materials Research Society Proceedings, Spring (2014)

[59] R. Swanepoel, “Determination of surface roughness and optical constants of inhomogeneous amorphous silicon films”, Journal of Physics E (Scientific Instruments) 17.10, 896 (1984)

[60] Z. Iqbal and S. Veprek, “Raman Scattering From Hydrogenated Microcrystalline and Amorphous Silicon”, Journal of Physics C, 15(2), 377-392 (1982)

[61] E. Bustarret, M. A. Hachicha, and M. Brunel, “Experimental determination of the nanocrystalline volume fraction in silicon thin films from Raman spectroscopy.” Applied Physics Letters 52.20, 1675-1677 (1988)

[62] T. Walter, R. Herberholz, C. Muller and H. Schock, “Determination of defect distributions from admittance measurements and application to Cu(In,Ga)Se2 based heterojunctions”, Journal of Applied Physics 80, 4411-4420 (1996)

[63] S. Kajjam, “Influence of Oxygen on Electronic properties of Nanocrystalline Silicon”, PhD Thesis, Iowa State University (2013)

[64] S. Kajjam, S. Konduri, M. Noack, G. Shamshimov, N. Ussembayev and V. Dalal, “Defect Densities and Carrier Lifetimes in Oxygen doped Nanocrystalline Si”, Materials Research Society Proceedings, 1536, 169-173 (2013)

[65] J. Heath and P. Zabierowski, “Capacitance Spectroscopy of Thin-Film Solar Cells”, Advanced Characterization Techniques for Thin Film Solar Cells (Wiley-VCH), 81-105 (2011)

[66] S. Kajjam, S. Konduri and V. Dalal, “Influence of oxygen contamination on minority carrier lifetime and defect density in nanocrystalline Si”, Applied Physics Letters, 103, 093506 (2013)

[67] S. S. Hegedus and E. Fagen, “Midgap states in a-Si:H and a-SiGe:H pin solar cells and Schottky junctions by capacitance techniques”, Journal of Applied Physics 71, 5941-5951 (1992)

[68] H. J. Scofield, “Effects of series resistance and inductance on solar cell admittance measurements”, Solar energy materials and solar cells 37.2, 217-233 (1995)

[69] J. A. Carr, “The identification and characterization of electronic defect bands in organic photovoltaic devices”, PhD Thesis, Iowa State University (2014)

[70] J. D. Cohen and D. V. Lang, “Calculation of the dynamic response of Schottky barriers with a continuous distribution of gap states”, Physical Review B 25 (8), 5321 (1982)

APPENDIX

DEFECTS AND DOPING IN NANOCRYSTALLINE SILICON-GERMANIUM DEVICES

This work was published in MRS proceedings 2014.

Siva Konduri, **Watson Mulder**, and Vikram L. Dalal

Department of Electrical and Computer Engineering, Iowa State University, Ames, Iowa

ABSTRACT

Nanocrystalline Silicon-Germanium (Si,Ge) is a potentially useful material for photovoltaic devices and photo-detectors. Its bandgap can be controlled across the entire bandgap region from that of Si to that of Ge by changing the alloy composition during growth. In this work, we study the fabrication and electronic properties of nanocrystalline devices grown using PECVD techniques. We discovered that upon adding Ge to Si during growth, the intrinsic layer changes from n-type to p-type. We can change it back to n-type by using ppm levels of phosphorus, and make reasonable quality devices when phosphine gas was added to the deposition mix. We also measured the defect density spectrum using capacitance-frequency techniques, and find that defect density decreases systematically as more phosphine is added to the gas phase. We also find that the ratio of Germanium to Silicon in the solid phase is higher than the ratio in the gas phase.

INTRODUCTION

Nanocrystalline Si (nc-Si) is an important and useful material for solar cells and photo-detectors. Significant progress has been made in the solar conversion of efficiency of nc-Si

with efficiencies exceeding 10% in single junction cells, and exceeding 15% in multiple junction cells [1-5]. However, there has been little progress in increasing the efficiencies of nanocrystalline (Si,Ge) alloys [6-10], which can potentially achieve high quantum efficiencies in the infrared range out to 0.68 eV, i.e. the bandgap of crystalline Ge. It is usually found that as one adds Ge to Si, the device performance becomes worse, and it has been speculated that this decrease in performance is due to additional Ge-associated defects in the material [10, 11]. In this paper, we show that addition of Ge to Si leads to significant increases in defect density, and may even make the intrinsic n-layer material become p-type. We also show that addition of ppm levels of phosphorus, using phosphine, to the intrinsic layer reduces the defect density and makes the material n-type again, and allows one to achieve reasonable devices with quantum efficiencies extending further into the infrared regions.

EXPERIMENTS

The materials and devices were fabricated using PECVD techniques using a VHF plasma at ~47 MHz. The substrate temperature was in the range of ~250 °C and pressure was ~ 100mT. The precursor gases were hydrogen, silane and 10% germane diluted in hydrogen. Varying levels of Ge:Si could be produced by varying the germane to silane flow ratio. Ppm levels of dopants such as phosphorus and boron could be introduced in the base (intrinsic) layer using dopant gases such as phosphine and diborane diluted in hydrogen. The devices were standard p+/i/n+ devices, deposited on pre-cleaned stainless steel substrates with the i-layer generally being n-type for nc-Si. ITO dots are deposited as top contacts and the contact area is 0.12 cm^2. SiGe is used as p-layer to avoid kinks in bandgap and a smooth transition at p-i interface and Ge concentration in p-layer is around 20%. The basic device structure of nc-SiGe:H solar cell is shown in Fig. 1. Thickness of i-layer is about 0.70 μm.

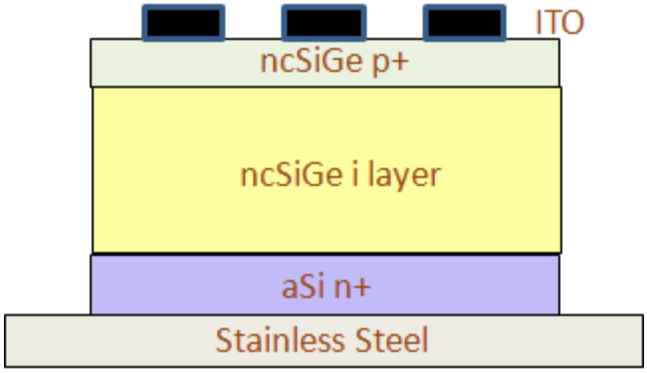

Figure 1. Typical device structure of nc-SiGe:H solar cell

For measuring defect densities, we used the capacitance-frequency techniques described previously [12]. Device quantum efficiency (QE) was also measured using standard techniques. The ratio of Ge:Si in the solid phase was determined using energy dispersive x-ray spectroscopy.

RESULTS

In Fig. 2, we show the ratio of Ge:Si in the solid phase for various germane:silane flow rates. It is clear from this figure that much more Ge is incorporated in the solid phase as than is present in the gas phase.

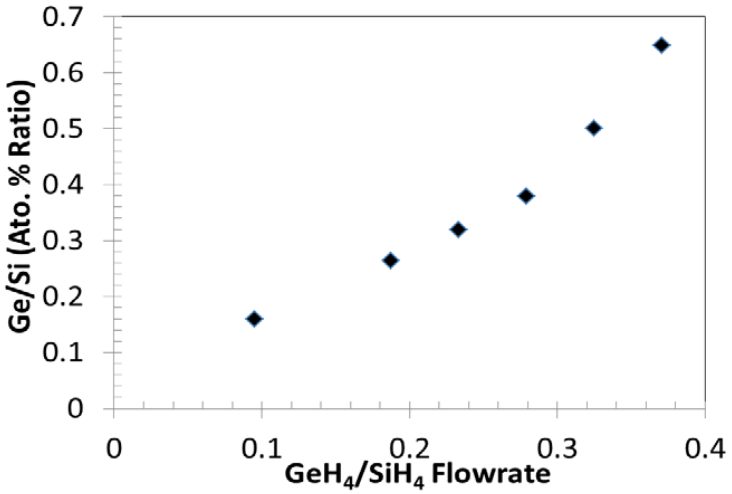

Figure 2. Germanium content for different gas flows in nc-SiGe:H devices

In Fig. 3a, we show the illuminated I-V curves for samples prepared using varying germane:silane ratios. A surprising result is that the short-circuit current actually decreases as the germane content in the gas phase increases. This is in spite of the fact that the germane:silane ratio in the solid phase is increasing, thereby implying a smaller bandgap material for higher germane flows. The explanation for this behavior is provided by studying quantum efficiency data, shown in Fig. 3b. It is clear from the QE data that there is a drastic reduction in QE for short wavelengths when significant amounts of germane are added to the input gas mixture. This can be ascribed to poor collection of electrons being generated near the p-n interface by light of shorter wavelengths, i.e. to a drastic reduction in electron diffusion length. This could be a result of the n-type intrinsic layer changing to a p-type, presumably due to Ge defects absorbing electrons from the oxygen induced donor states [13]. Indeed, there appears to be a significant increase in defect density when Ge content increases. See Fig. 4 for data on defect density vs. energy for varying German:Silane flow rates.

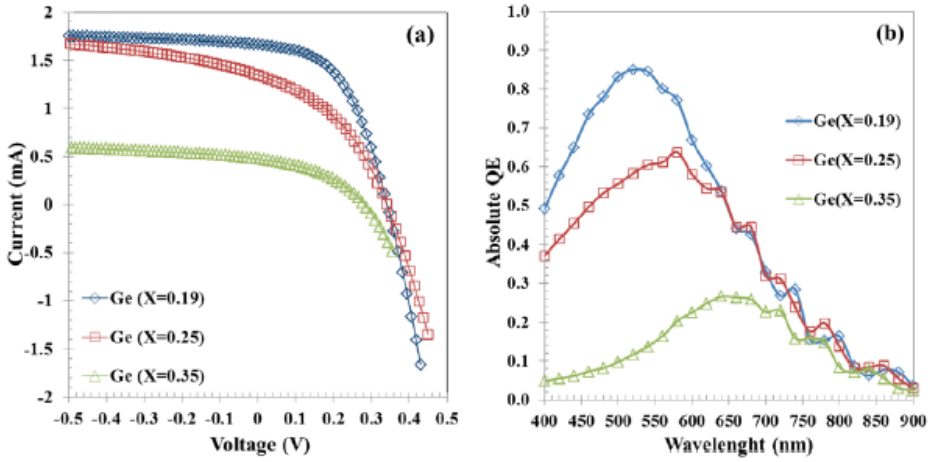

Figure 3. (a) IV curves and (b) Absolute QE vs. Wavelength for nc-SiGe:H solar cells with varying Ge content

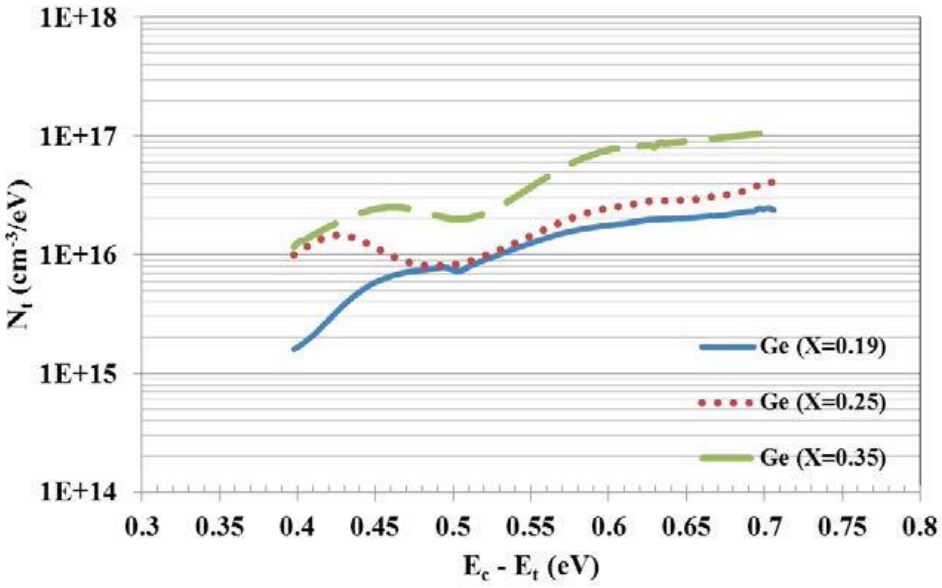

Figure 4. Calculated defect density vs. energy below the conduction band for varying Ge content

To overcome the deleterious effects of additional Ge on both defect density and QE, we tried to compensate for the apparent p-type doping by adding ppm levels of PH_3 to the gas mixture. The results for I-V curves are shown in Fig. 5a for various values of PH_3 for a fixed germane:silane ratio of in the gas phase. Clearly, adding PH_3 significantly improves the short-circuit current in the solar cell. The corresponding QE curves are shown in Fig. 5b, and they clearly show an improvement in QE at short wavelengths, compared to the QE curves shown in Fig. 3, thus showing that the poor electron collection efficiency for photons which are absorbed near the p-intrinsic layer interface has been overcome. The corresponding change in total defect density as a function of PH_3 flow is shown in Fig.6, thus confirming that addition of ppm levels of PH_3 serves to reduce the defect density in nanocrystalline (Si,Ge) intrinsic layers, probably by compensating the defects caused by Ge addition.

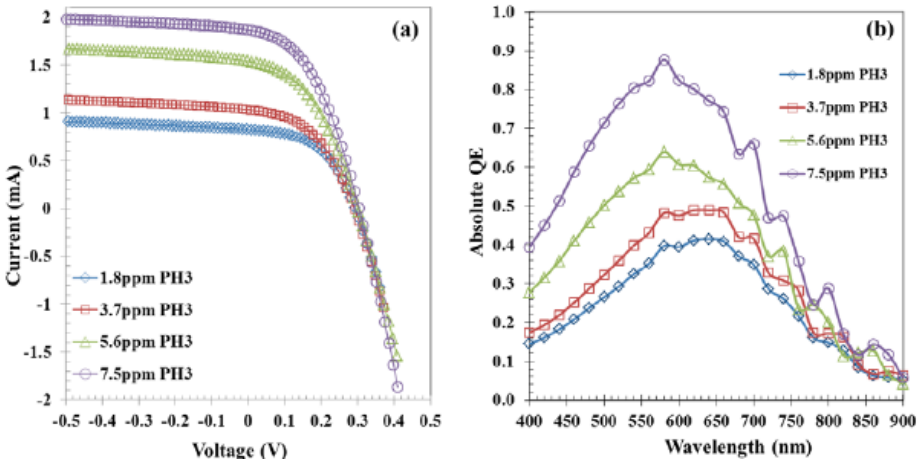

Figure 5. (a) IV curves and (b) Absolute QE vs. Wavelength for nc-SiGe:H solar cells with (X_{Ge}~0.35) for varying PH_3 flow rates

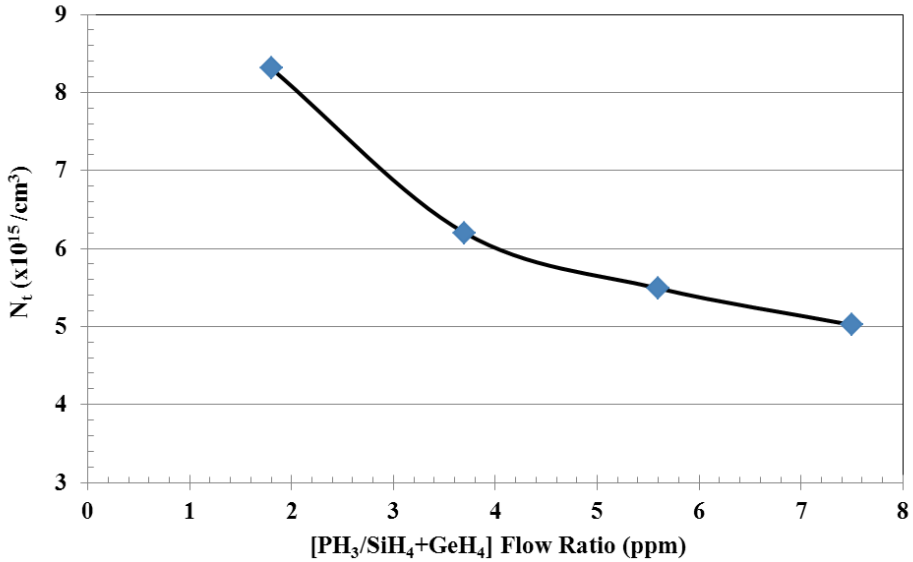

Figure 6. Total defect density as a function of PH_3 flow rate

IV curves for the devices prepared using varying ratios of germane:silane flow along with optimum ppm levels of PH_3 are plotted in Fig.7a, which clearly show that increasing Ge content leads to higher short-circuit currents but approximately the same open-circuit voltage. In general, V_{oc} depends on quality of i-layer, type of p-layer, and transition layers. Further experiments are being conducted to examine the relationship of V_{oc} with Ge content. The corresponding QE data in Fig. 7b shows that increasing Ge content shifts the curves to longer wavelengths, as expected.

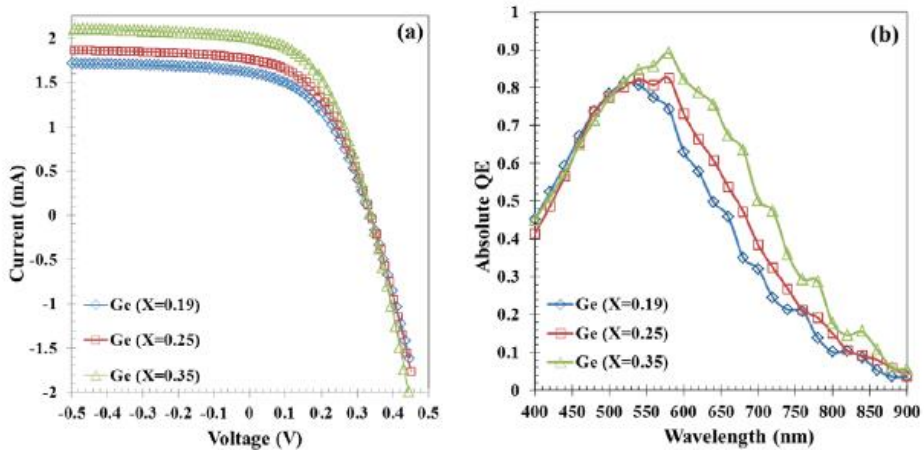

Figure 7. (a) IV curves and (b) Absolute QE vs. Wavelength for nc-SiGe:H solar cells with varying Ge content with optimum PH_3 flow (i-layer Thickness ~ 0.7μm)

CONCLUSIONS

In conclusion, we have shown that the defect density in the intrinsic layer of nanocrystalline p-i-n solar cells material increases significantly as Ge content increases. It appears that adding Ge changes the doping type of the intrinsic layer form n-type to p-type. This shift leads to a drastic reduction in quantum efficiency for short wavelength photons at higher Ge concentrations. The defect density can be reduced, and the p-type behavior changed back to n-type by adding ppm levels of PH_3 to the gas phase. The results show that when appropriate compensation by Phosphorus has been achieved, the quantum efficiency for solar cells extends further out towards longer wavelengths as the Ge content of the solar cell intrinsic layer increases, as expected, resulting in larger currents. This is an important result which shows that nanocrystalline (Si,Ge) cells can be used to improve the efficiency of tandem junction solar cells, as also the infrared response when these materials are used as photo-detectors.

ACKNOWLEDGMENTS

It is a pleasure to acknowledge the technical help of Andrew Gulstad and Max Noack. This work was partially supported by a grant from NSF.

REFERENCES

1. J. Meier, R. Flückiger, H. Keppner and A. Shah, Applied Physics Letters, **65**, 860-862 (1994)

2. A. Shah, J. Meier, E. Vallat-Sauvain, C. Droz, U. Kroll, N. Wyrsch, J. Guillet and U. Graf, Thin Solid Films, **403–404**, 179-187, (2002)

3. A. Shah, J. Meier, E. Vallat-Sauvain, N. Wyrsch, U. Kroll, C. Droz and U. Graf, Solar Energy Materials and Solar Cells, **78**, 469-491, (2003)

4. V. Dalal, J. Leib, K. Muthukrisnan, D. Stieler, and M. Noack, 2005 IEEE Photovoltaic Specialists Conference, 1448- 1451, (2005)

5. G. Yue, B. Yan, L. Sivec, T. Su, Y. Zhou, J. Yang and S. Guha, 2012 MRS Proceedings, **1426**, 33-38, (2012)

6. M. Isomura, K. Nakahata, M. Shima, S. Taira, K. Wakisaka, M. Tanaka and S. Kiyama, Solar Energy Materials and Solar Cells, **74** (1–4), 519-524 (2002)

7. J. K.Rath, F.D. Tichelaar and R. E.I Schropp, Solar energy materials and solar cells, **74,** 553-560 (2002)

8. S. Saripalli and V. Dalal, EIT 2008 IEEE International Conference Proceedings, 414-418, (2008)

9. T. Matsui, M. Kondo, K. Ogata, T. Ozawa and M. Isomura, Applied Physics Letters, **89**, 142115, (2006)

10. T. Matsui, K. Ogata, C.W. Chang, M. Isomura and M. Kondo, Journal of Non-Crystalline Solids, **354** (19–25), 2468-2471, (2008)

11. T. Matsui, C.W. Chang, T. Takada, M. Isomura, H. Fujiwara and M. Kondo, Solar Energy Materials and Solar Cells, **93**, 1100-1102, (2009)

12. K. Shantan, K. Siva and V. Dalal, Applied Physics Letters, **103**, 093506 (2013)

13. T. Matsui, C.W. Chang, K. Mizuno, Y. Takeuchi and M. Kondo, Japanese Journal of Applied Physics, **51,** 091302, (2012)